Photocurrents in topological insulator
nanowire and Hall bar devices

I n a u g u r a l d i s s e r t a t i o n

zur

Erlangung des akademischen Grades eines

Doktors der Naturwissenschaften (Dr. rer. nat.)

der

Mathematisch-Naturwissenschaftlichen Fakultät

der

Universität Greifswald

vorgelegt von

Nina Meyer

geboren am 07.12.1991

in Buchholz i. d. N.

Greifswald, 18.01.2021

Dekan:	Prof. Dr. Gerald Kerth
1. Gutachter:	Prof. Dr. Markus Münzenberg
2. Gutachter:	Prof. Dr. Alexander Holleitner
Tag der Disputation:	26.03.2021

Contents

1 Exposé

1.1 Introduction

In this thesis, the transport properties of a special phase of condensed matter - the so called topological insulator - are investigated. Like an ordinary insulator, a topological insulator has a bulk energy gap separating the highest occupied electronic band from the lowest unoccupied band. In contrast to a trivial insulator, the bulk band gap of the topological insulator is closed by boundary states leading to a conducting state at the surface.
Topological insulators are based on a fundamental connection between the insulating bulk and conducting surface states. The so-called bulk-boundary correspondence relates the conducting surface states to the non-trivial topology of the bulk bands, which explains the robustness of the surface states against imperfections [1–4]. Depending on the spatial dimensionality and symmetry of the system, various different types of topological insulators can arise [5]. Here, we focus on three-dimensional topological insulators with time-reversal symmetry. This material class was predicted in 2006 [6–8]. The name "topological insulator" was coined by Moore and Balents [7] and the connection between the bulk topology and the existence of conducting surface states was established by Fu, Kane and Mele [6]. After the theoretical prediction, $Bi_{1-x}Sb_x$ was discovered as the first three-dimensional topological insulator, followed by the discovery of the "second generation" of three-dimensional topological insulators consisting of Bi_2Se_3, Bi_2Te_3 and Sb_2Te_3 [9–11].
A topological insulator is distinguished from a trivial insulator by non-zero values of topological invariants that are assigned to the bulk bands. The materials used in this thesis belong to the second generation of three-dimensional topological insulators, which are characterized by a $\mathbb{Z}_2$ invariant ν_0 [6]. For $\nu_0 = 1$, the bulk bands possess a non-trivial topology. This implies, in the simplest case, that the conducting surface states form a single Dirac cone in the two-dimensional surface Brillouin zone. Consequently, the surface states have a linear dispersion like massless Dirac fermions. They are also helical, i.e., electrons with opposite momenta have opposite spins. In addition, the surface states are Kramers degenerate at a time-reversal invariant momentum $k \equiv -k$ (modulo a reciprocal lattice vector). The point where Kramers degeneracy is enforced is called Dirac point. This results from the time-reversal symmetry according to which the surface states must appear in Kramers pairs at momentum k and $-k$ with opposite spins. Thus, backscattering from k to $-k$ is forbidden, provided that no time-reversal-breaking perturbations are introduced in the system and the bulk energy gap does not close. The surface states are therefore called topologically protected.
In real materials, the surface states can be probed experimentally by scanning tunneling microscopy. In this way, the linear dispersion relation and the suppressed backscattering of the surface states can be detected [12–14]. Topological insulator materials can also

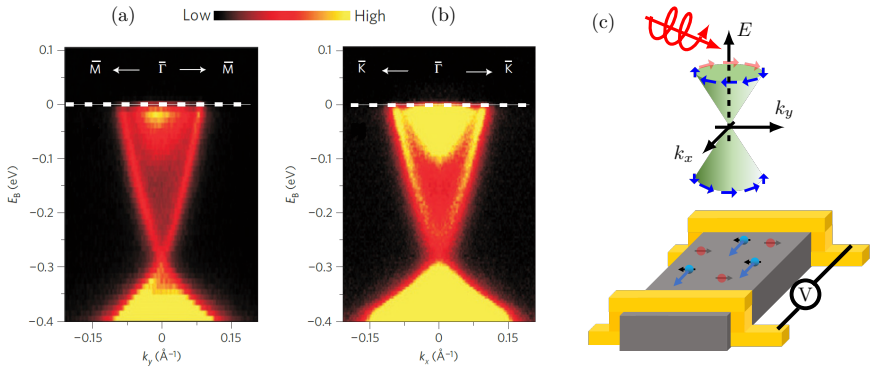

Figure 1.1: (a,b) ARPES measurements of the surface electronic band dispersion on Bi_2Se_3 (111) are displayed. The electron dispersion data measured near the Γ-point along the (a) Γ–M and (b) Γ–K momentum-space cuts are shown. Adapted from [11]. (c) The spin-polarized current due to the circular photogalvanic effect.

be identified by measuring their band structure through angle-resolved photoelectron spectroscopy (ARPES) [11, 15–17]. An example of the obtained band structure for Bi_2Se_3 (111), which is used for the nanowires in this thesis, is provided in Fig. 1.1. The crossing of the surface states forming the Dirac point at the Γ point and the linear dispersion close to the Dirac point within the bulk band gap of 300 meV are visible [11]. The spin orientation of the surface states can be verified by using spin-resolved ARPES [15], by discussing the circular dichroism [18], or by using ultrafast laser spectroscopy to measure the magneto-optical Kerr rotation [19, 20].

The intense attention brought towards topological insulators is based on the helical surface states and their protection against elastic backscattering. Due to the spin-momentum locking, every charge current flowing at the surface is spin-polarized. This makes topological insulators a promising material class for the field of spintronics.

Exciting photocurrents at the surface of a topological insulator is one of the possibilities to generate and control spin-polarized currents. This was first demonstrated experimentally by McIver et al. [21] for Bi_2Se_3 at room temperature. They detected a sign change in the photocurrent depending on the helicity of the excitation light. This observation can be explained with the circular photogalvanic effect (CPGE), which was predicted by Ivchenko, Pikus [22], and Belinicher [23] and first observed in GaAs/AlGaAs quantum wells by Ganichev et al. [24, 25]. This effect denotes the process in which illumination of a material with circular-polarized light generates an asymmetric carrier population in the k-space which causes a spin-polarized current flow. When a topological insulator is illuminated with circular-polarized light, the light couples to spins which are aligned or antialigned to the wave vector of the light depending on the polarization of the light [26]. For the polarization chosen in Fig. 1.1(c), electrons with a spin component parallel to the wave vector ($+k_y$, red) are transferred to higher energies in the band structure. The electrons with a spin component in $-k_y$-direction (blue) are generally not excited and thus, dominate the surface state population. This asymmetric population causes a spin-polarized charge current, see Fig. 1.1(c). Changing the helicity of the laser light inverts the direction of the current flow.

The CPGE has been exploited in a variety of photocurrent measurements on three-dimensional topological insulators, which differ by the excitation wavelength, pulse rate and choice of material [27–31]. Kastl et al. [27], for example, used ultrafast laser pulses within the visible range to separate the helicity-dependent photocurrents at the surface from the polarization-independent photocurrents on a picosecond time scale. They demonstrated that the direction of the spin-polarized currents is helicity-dependent. Okada et al. [28] used laser light with a wavelength in the near infrared regime for their photocurrent experiments on a series of $(Bi_{1-x}Sb_x)_2Te_3$. Here, the parameter x defines the position of the Fermi energy with respect to the Dirac point. They observed that the CPGE increases when the Fermi energy is close to the Dirac point. Braun et al. [30] used femtosecond laser pulses to generate terahertz radiation by illuminating Bi_2Se_3. They discovered, that the helicity-dependent photocurrent is dominated by an ultrafast charge transfer along the Se–Bi bonds.
In this thesis, we investigate the spatial distribution of the photocurrent by scanning large areas of the sample surface with a small laser spot and measuring the induced photocurrent at each laser spot position. In this way, the influence of the substrate, the contacts, and the edges of the topological insulator on the spin-polarized current can be deduced from the experimental data. Our measurement setup is introduced in Sec. 1.2. Two types of samples are investigated. Namely, Bi_2Se_3 nanowires and $(Bi_{0.57}Sb_{0.43})_2Te_3$ Hall bar devices. These devices differ by their topological insulator material and their physical dimensions.
Most of the measurements reported so far use ultrathin topological-insulator crystals or grown thin films. Although their thickness can be 8 nm or larger, their width, even when structured into Hall bar devices, is in the micrometer range. For nanowires, the surface-to-volume ratio is significantly larger. This enhances the contribution of the surface states to the photocurrent relative to the bulk contribution. Thus, the main focus in this thesis is the generation of spin-polarized currents in topological nanowires. To actually obtain the spin-polarized current from the photocurrent data, it has to be separated from other current contributions, like the thermoelectric current, by exploiting the polarization of the excitation beam. This is discussed in detail in Sec. 1.3. In this way, we can demonstrate for the first time the generation and optical control of spin-polarized currents in Bi_2Se_3 nanowires (see article I).
At the interface between the metallic contacts and the topological nanowire, we observe a strong enhancement of the spin-polarized current as well as the thermoelectric current (see article II). This phenomenon is reproduced for various different nanowires and contact geometries in Sec. 1.4. A similar enhancement of the spin-polarized current is observed at the edges of the Hall bar devices (see article III). We find that the enhancement of the thermoelectric current can be explained with the Schottky effect (see Sec. 1.5). The enhancement of the spin-polarized current, on the other hand, is correlated with the spatial distribution of the thermoelectric current. Differences in the spatial distribution indicate the occurrence of temperature gradients which cause spin-dependent deflections of the surface electrons via the spin Nernst effect (see Sec. 1.6).
In total, our results show that the spatial distribution of both current contributions - the spin-polarized and the thermoelectric current - are necessary to gain a deeper understanding of the generation of spin-polarized currents in topological insulators.

1.2 Measurement setup and technique

This section describes the samples and the experimental setup for the photocurrent measurements. The measurements are done on either Bi_2Se_3 nanowires or $(Bi_{0.57}Sb_{0.43})_2Te_3$ Hall bar devices. A representative microscope image of each sample is displayed in Fig. 1.2.
The Bi_2Se_3 nanowires are grown by the gold-nanoparticle-assisted catalytic vapor liquid solid method. Further information on the fabrication of the nanowire and various transport measurements which indicate the existence of topologically-protected surface states can be found in refs. [32, 33]. The $(Bi_{0.57}Sb_{0.43})_2Te_3$ thin films are grown using molecular-beam epitaxy. Afterwards, they are structured into Hall bar devices by using optical lithography and Ar^+dry etching [34]. The ratio of bismuth and antimony defines the relative position of the Fermi level compared to the Dirac point in the band gap [35]. The doping of the topological layer changes from n-doped to p-doped when the antimony content increases from 0% to 100%. At around 43% of antimony, the Fermi level crosses the Dirac point and the compensation point is reached. Hence, the topological insulator that is used for the Hall bar devices in this thesis is intrinsic [34, 36]. In this way, the bulk charge-carrier concentration is reduced to $2 \cdot 10^{20}\,\mathrm{cm}^{-3}$, while the carrier concentration of the surface states is on the order of $3 \cdot 10^{13}\,\mathrm{cm}^{-2}$ [34, 35, 37].
The setup displayed in Fig. 1.3 is used for the photocurrent measurements on the Hall bar and nanowire devices. It consists of an optical part, which generates the photocurrent $j(\alpha)$ at a controlled position on the sample and an electrical detection part. The light source is a cw diode laser with a wavelength $\lambda = 785\,\mathrm{nm}$ modulated at $f = 77\,\mathrm{Hz}$ by a square-function generator. The corresponding photon energy $E_{\mathrm{photon}} = 1.55\,\mathrm{eV}$ is larger than the bulk band gap. Thus, transitions from the surface states to the bulk states and from the valence band to the conduction band in the bulk are possible. The possible transitions between the bulk bands do not contribute to the spin-polarized current, since the associated states do not possess a linear dispersion. The CPGE is exclusively driven by the depopulation of the surface states.
After leaving the diode laser, the laser beam passes a half-wave plate (HWP) to control the laser power and two lenses, which form a Kepler telescope to minimize the divergence of the laser beam. Afterwards, the laser beam is guided through a linear polarizer combined with a rotatable quarter-wave plate (QWP) for polarization control before

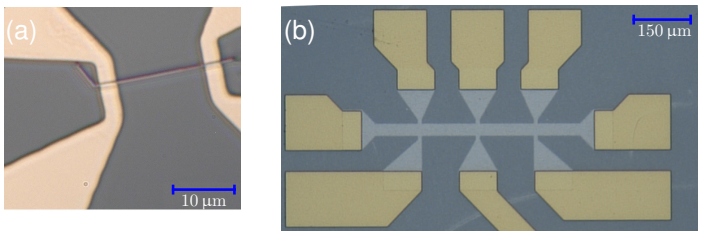

Figure 1.2: Microscope image of (a) a Bi_2Se_3 nanowire on Si/SiO substrate (gray areas) with two gold contacts (yellow areas) placed on top of the nanowire and (b) a $(Bi_{0.57}Sb_{0.43})_2Te_3$ Hall bar device on Si (111) (dark gray areas) with gold contacts (yellow areas) on top. Adapted from articles II and III, Sec. 3.3 and Sec. 3.4.

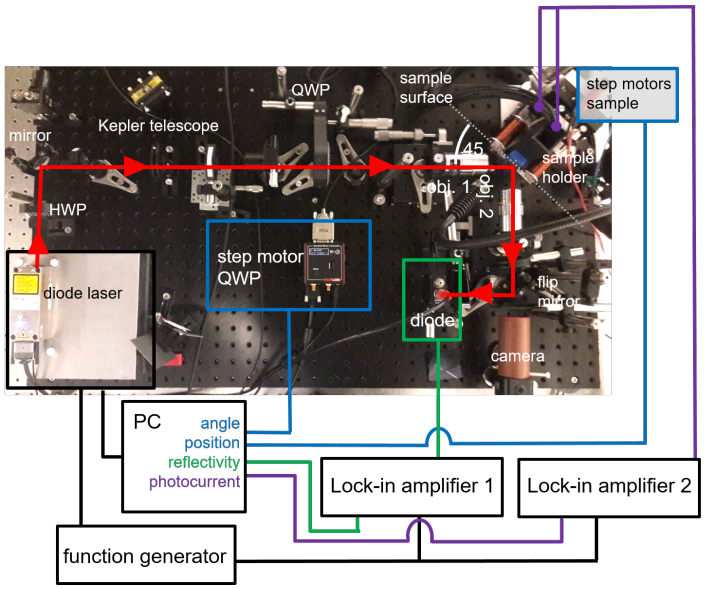

Figure 1.3: The experimental setup with its optical (picture) and electric (sketched on top of the picture) components. The various colors mark the different recorded parameters of the measurement and the path of the laser light.

impinging on the sample surface at an angle of incidence of $\theta = 45°$. The power density on the sample surface is $P_{\text{linear}} \approx 200\,\text{W/cm}^{-2}$. The QWP is characterized before and after every measurement, which allows us to identify the polarization of the laser light by measuring the rotation angle α of the QWP during the photocurrent experiment. The QWP is characterized by placing it between two linear polarizers and measuring the laser power behind the second polarizer. The linear polarizers are arranged in such a way that their transmission axes are perpendicular to each other. Consequently, the measured power is zero when the QWP generates linear polarized light with an oscillation plane perpendicular to the transmission axis of the second linear polarizer. This is the case for $\alpha = n \cdot 90°$ (see Fig. 1.4) with integer n. The QWP emits circular polarized light when the laser power reaches its maximum at an angle of $\alpha = 45° + n \cdot 90°$. Taking into account the position of the fast axis on the QWP, left- and right-circular polarized light is generated at the angles specified in Fig. 1.4.
The laser light is focused to a spot size of 2.90(8) µm × 3.40(12) µm (full width at half maximum (FWHM) along the horizontal and the vertical direction) on the sample surface. The exact spot size in each measurement differs by less than 1 µm for every measurement on a different sample. This is due to the elliptical shape of the laser spot on the sample surface and the orientation of the edge chosen for the knife-edge method [38] to determine the spot size. When the orientation of the edge changes, the orientation and size of the two measured laser spot axes changes, while the shape of the ellipse remains constant.
After the laser light impinges on the sample, the reflected intensity $I_{\text{ref}}(\alpha)$ is collimated by a second objective. The laser light is either recorded by a CCD camera or reflected by a flip mirror and recorded by a photodiode. The later case is sketched in Fig. 1.3. The CCD camera, in combination with a lamp which illuminates the sample surface,

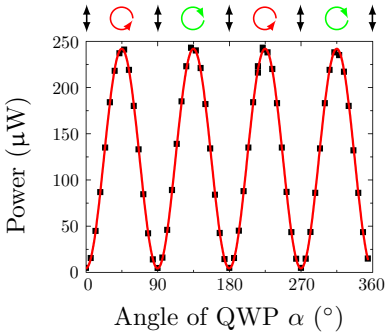

Figure 1.4: Characterization of the quarter-wave plate (QWP). The arrows on top indicate the polarization of the laser light behind the QWP. Adapted from article I, sec 3.2.

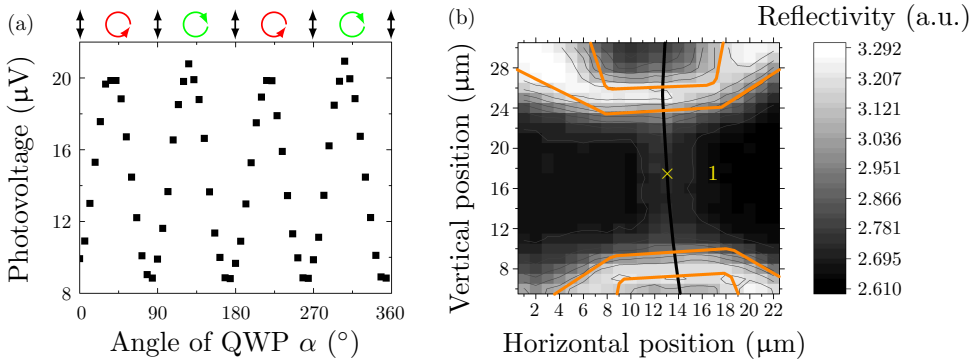

Figure 1.5: (a) The photovoltage $v(\alpha)$ measured on the nanowire at position 1 in Fig. 1.5(b). (b) Reflectivity map with the outline of the contacts (orange lines) and the nanowire (black line). The yellow cross marks the position where the photovoltage $v(\alpha)$ in Fig. 1.5(a) is measured. Adapted from article I, sec 3.2.

enables the observation of the laser spot and a small area of the sample at the same time. Thus, the position of the laser spot can be monitored while the laser spot is moved to the starting point of the scans via the two step motors attached to the sample holder (see Fig. 1.3). During the photocurrent measurements, the photodiode is used to detect the reflected intensity $I_{\mathrm{ref}}(\alpha)$ simultaneously with the photocurrent $j(\alpha)$. This allows us to distinguish areas with different refractive indices like the gold contact from the silicon substrate in Fig. 1.5(b).

The photocurrent $j(\alpha)$ of the sample and the reflected intensity $I_{\mathrm{ref}}(\alpha)$ are detected with lock-in amplifiers, which are based on the phase-sensitive detection of an ac-signal. The periodically-generated photocurrent $j(\alpha)$ is measured with the frequency of the function generator $f = 77\,\mathrm{Hz}$ as the reference frequency, which increases the signal to noise ratio. Depending on which lock-in amplifier input is used, either a photocurrent $j(\alpha)$ or a photovoltage $v(\alpha)$ is detected. We observed that the quality of our measurements is unaffected by the choice of the lock-in amplifier input. In the following, we will show representative results for both the photocurrent and photovoltage measurements.

The measured photocurrent $j(\alpha)$ is mapped to the polarization state of the excitation light via the QWP's rotational angle α at a fixed position (m, n). The QWP is rotated

at every laser spot position (m, n) from $\alpha = 0°$ to 360° with a step size of $\Delta\alpha = 6°$. This generates a set of 60 values for each position (m, n), as presented in Fig. 1.5(a), as well as 60 values for the reflected intensity $I_{\mathrm{ref}}(\alpha)$. The spatially-resolved maps of the reflected intensity and photocurrent are obtained by moving the laser vertically and horizontally across the sample with the step motors in a defined area. The laser spot positions (m, n) are arranged in a equidistant grid. For the nanowire samples, the distance in the vertical and horizontal direction is $\Delta m = \Delta n = 1\,\mu\mathrm{m}$.
The reflected intensity is mapped to the position of the laser spot by taking one value for $\alpha = 0°$. In this way, the reflected intensity can be displayed as a two-dimensional map to reveal the positions of the gold contacts, topological insulator, and the silicon substrate as shown in Fig. 1.5(b).
For the analysis of the photocurrent, it is necessary to identify its individual contributions. The different contributions are determined via their polarization-dependence at every laser spot position. The results are then summarized in the two-dimensional maps. The different photocurrent contributions are discussed in the next section.

1.3 Photocurrent contributions

The photocurrent can be described phenomenologically via a taylor expansion in the power of the electric field $\vec{E}(\omega, \vec{q})$ of the excitation beam at the frequency ω and the photon momentum $\vec{q}$ inside the material [25]. The electric field is assumed to be a plane wave $\vec{E}(\vec{r}, t) = \vec{E}(\omega, \vec{q}) \exp(-i\omega t + i\vec{q}\vec{r}) + \vec{E}^*(\omega, \vec{q}) \exp(+i\omega t - i\vec{q}\vec{r})$. In the following, the amplitude $\vec{E}(\omega, \vec{q})$ is written as E_μ. The lowest non-vanishing order of the expansion yields the DC current density j_λ described by [25, 39]

$$\begin{aligned} j_\lambda &= \sigma_{\lambda\mu\nu} E_\mu E_\nu^* \\ &= \chi_{\lambda\mu\nu} E_\mu E_\nu^* + \mathrm{T}_{\lambda\delta\mu\nu} q_\delta E_\mu E_\nu^* + c.c.\ , \end{aligned} \tag{1.1}$$

where summation over repeated indices $\lambda, \mu, \nu, \delta$ is implied. The index λ can be the x- or y-direction on the sample surface and the indices μ and ν run over the cartesian coordinates x, y, and z. $\sigma_{\lambda\mu\nu}$ is the third-rank photocurrent conductivity tensor. $\chi_{\lambda\mu\nu}$ and $\mathrm{T}_{\lambda\delta\mu\nu}$ are third-rank and fourth-rank tensors. The first term in Eq. (1.1) describes the photogalvanic effect and the second term describes the photon drag effect. The latter depends on the photon momentum, while the first one does not. Both effects can be expanded further into a circular and a linear contribution by splitting the tensors into real and imaginary parts. The resulting expressions can be found in refs. [39, 40]. Due to symmetry restrictions, the photogalvanic effect can only occur in non-centrosymmetric materials. Thus, it occurs on the surface of Bi_2Se_3 and $(Bi_{0.57}Sb_{0.43})_2\,Te_3$ but not in the bulk [29]. The photon drag effect occurs both in the bulk and on the surface.
Taking into account the crystal symmetry of the sample surface and the polarization of the excitation beam as a function of the angle α, the photocurrent can be described phenomenologically by [21, 41]

$$j(\alpha) = C\sin(2\alpha) + L_1\sin(4\alpha) + L_2\cos(4\alpha) + D\ . \tag{1.2}$$

The parameters C, L_1, L_2, and D are the amplitudes of different current contributions. In Bi_2Se_3, this functional dependence was first observed by McIver et al..

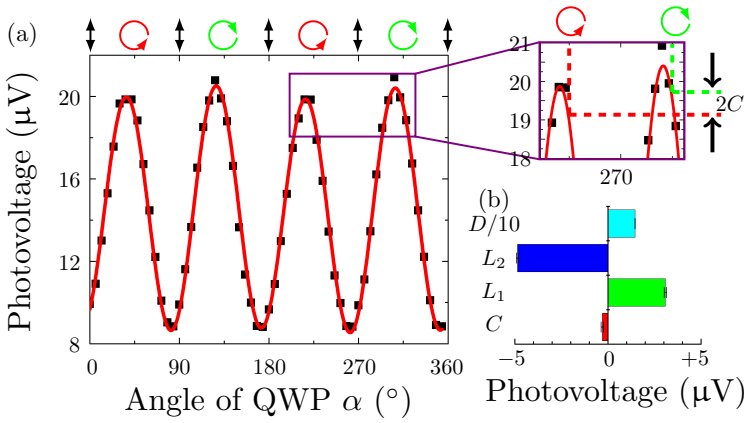

Figure 1.6: (a) The photovoltage $v(\alpha)$ (black squares) measured on the nanowire at position 1 in Fig. 1.5(b). The data is fitted to Eq. (1.2). (b) The values for C, L_1 , L_2, and D and their uncertainties from the fit are displayed as a bar chart. Adapted from article I, sec 3.2.

The first term $C\sin(2\alpha)$ of Eq. (1.2) modulates the difference in the photocurrent for left- and right-circular polarized light and is zero if the excitation light is linear polarized. The amplitude C is half the difference between the photovoltages for opposite helicities (see Fig. 1.6(a)). The first term is the only one in Eq. (1.2) that is influenced by the helicity of the circular polarized light. The physical mechanism that generates the helicity-dependent photocurrent is still under discussion. One candidate for this mechanism is the circular photogalvanic effect, as suggested by photocurrent measurements on Bi_2Se_3 crystals by McIver et al. [21]. A second candidate is the so called circular photon drag effect (CPDE). This effect has been observed by Shalygin et al. [42] in (110)-grown quantum wells. The difference between these two effects will be discussed in Sec. 1.3.1. The second term $L_1\sin(4\alpha)$ and the third term $L_2\cos(4\alpha)$ have the same frequency but are phase shifted. The second term is zero for linear- and circular-polarized light and reaches its extremal values for elliptic polarized light. The third term, on the other hand, reaches its extremal values for linear- and circular-polarized light and is zero for elliptic polarized light. Both current contributions are not spin-polarized and can arise from the linear photogalvanic effect and the linear photon drag effect [21, 43, 44]. Both contributions will not be addressed in the following, since the focus of this thesis is the generation and detection of spin-polarized currents.
The last term D in Eq. (1.2) is independent of the polarization. Hence, every polarization-independent absorption effect like the polarization-independent photogalvanic and photon drag effect can contribute to it. In addition, the laser light locally heats the sample, since the laser spot is smaller than the distance between the gold contacts. This creates a net temperature gradient that changes its direction and magnitude as the laser spot is moved across the sample surface. This temperature gradient generates a thermoelectric current, due to the Seebeck effect, which can also contribute to the parameter D. The physical origin of this parameter will be discussed in Sec. 1.3.2.
In the following, Eq. (1.2) is used as a fit function to determine the four parameter C, L_1, L_2, and D for each photocurrent measurement at every laser spot position (m, n) of the grid. One example for the measured photocurrent (black squares) and the

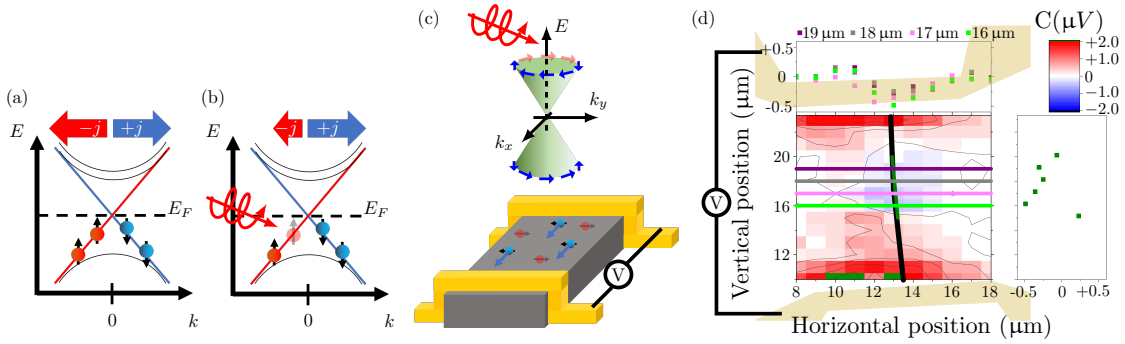

Figure 1.7: Band structure of a two-dimensional topological insulator. (a) The edge states are symmetrically populated. Thus, only spin currents but no charge currents flow along the edges. (b) Spin-up electrons are depopulated through absorption of circular-polarized light (red arrow). The asymmetrically-populated edge states generate a net spin-polarized charge current. (c) The asymmetric population of the Dirac cone for a three-dimensional topological insulator is depicted. The propagation direction (blue arrow) of the electrons remaining in the Dirac cone is depicted on a simplified sample (gray cuboid). (d) The map shows the spatially resolved amplitude C of the spin-polarized current. The vertical contour plot shows the values of C along the nanowire (dark green line) and the horizontal contour plots (violet, grey, pink, and light green lines) perpendicular to the nanowire. Adapted from article I, sec 3.2.

resulting fit function (red line) is provided in Fig. 1.6(a). The fit function (1.2) is in good agreement with the data. The values of the four parameters and their uncertainties are displayed in a bar chart in Fig. 1.6(b), showing that the parameter D is roughly one order of magnitude larger than L_1 and L_2 and roughly two orders of magnitude larger than the parameter C. The values for C, L_1, L_2, and D are then summarized for the whole measured area by displaying them as two-dimensional maps. An exemplary two-dimensional map of C is displayed in Fig. 1.7(d). The two axes represent the horizontal and vertical positions of the laser spot and the color indicates the sign and the value of the displayed amplitude. The focus of this thesis are the results for the parameter C, which is related to the spin-polarized current, and the amplitude D, which is polarization independent.

1.3.1 The spin-polarized current

There are several effects based on photon absorption, which generate polarization-dependent photocurrents. Here, we focus on two types of effects, which generate spin-polarized currents. Both effects are based on the absorption of circular polarized light, hence the word “circular” is added to their title. One effect cited as a possible origin for helicity-dependent photocurrents is the circular photon drag effect (CPDE), which represents an electrical current arising due to a simultaneous transfer of linear and angular momentum from the excitation photons to the free charge carriers in the solid [45–47]. A second effect is the circular photogalvanic effect (CPGE). This effect is based on an asymmetric population of the electrons in k-space, which causes a spin-polarized charge current. The asymmetric population is caused by interband transitions where the photon energy is absorbed according to the optical selection rules. The two effects differ

by their responses under inversion of the photon momentum $\vec{q}$. If the helicity-dependent term changes its sign when the sample is illuminated from the front and the back (i.e. $\vec{q} \rightarrow -\vec{q}$), the CPDE is the orgin of the first term in Eq. (1.2). If the sign remains unchanged, the CPGE is the cause of the contribution. In our setup, we can attribute the first term in Eq. (1.2) to the CPGE as in refs. [21, 31] so that the amount of spin-polarized current generated in the samples is determined by the parameter C.
The CPGE is well-known in semiconductors with lifted spin-degeneracy [24, 25]. In quantum wells, the asymmetric scattering of the charge electrons causes the asymmetric population. At the surface of a topological insulator, the spin-momentum locking forbids electron scattering between electrons with opposite spin orientations. But the spin-momentum locking opens up another way to generate spin-polarized currents based on the CPGE, as demonstrated in Fig. 1.7(a) and (b) for a two-dimensional topological insulator. When the topological insulator is not illuminated, the edge states are equally filled up to the Fermi energy for the two spin orientations (see Fig. 1.7(a)). Since the spin orientation is locked to the electron momentum, electrons with opposite spin propagate in opposite directions along the edges. Hence, there is no net charge transfer along the edges. Only a pure spin current flows along the edges. When the topological insulator is illuminated with circular polarized light, electrons are excited out of the edge states if the transition fulfills the optical selection rules. The helicity determines whether spin-up or spin-down electrons are excited. In the example in Fig. 1.7(b), left-circular polarized light excites spin-up electrons, which creates an asymmetric population of the edge states. Thus, the two counterpropagating spin currents at the edges transport an unequal amount of charge carriers, creating in total a spin-polarized charge current. For right-circular polarized light, the spin-polarized charge current flows in the opposite direction.
The Bi_2Se_3 nanowires and the $(Bi_{0.57}Sb_{0.43})_2\,Te_3$ Hall bar devices used in this thesis are three-dimensional topological insulators, since their thickness and width are larger than the hybridization limit for the surface states [48]. Even though the surface states are now two-dimensional and form a Dirac cone, spin-momentum locking still allows for the generation of spin-polarized charge currents. What changes is that the propagation direction of the excitation light now also influences the direction of the spin-polarized charge current. When left- (right-) circular polarized light illuminates the topological insulator, the electrons with a spin component parallel (antiparallel) to the incoming laser light are excited (see Fig. 1.7(c)). This creates an asymmetric population of the surface states, which generates a spin-polarized charge current propagating perpendicular to the plane of incidence. Changing the helicity of the circular-polarized light reverses the propagation direction of the spin-polarized current, as before. This reversal is encoded into the parameter C, since C is the difference between the photocurrent for left- and right-circular polarized light divided by two. Therefore, we expect that C has the same values at each nanowire position in our measurements.
The results for C derived from one measurement on a Bi_2Se_3 nanowire with a contact spacing of 14 µm are shown in Fig. 1.7(d). Here, the gold contacts are displayed in light orange. The size and the position of the gold contacts with respect to the nanowire are determined by comparing a microscope image of the sample with the reflected intensity in Fig. 1.6(b). The position of the nanowire, marked by a black line in Fig. 1.7(d), is identified in the same manner. In the middle of the nanowire, the amplitude C is negative

and approximately constant, as we expected. When the laser spot is moved closer to the contacts, C changes its sign and increases rapidly. The contour plot along the vertical dark green line confirms that the spin-polarized currents change significantly in the vicinity of the contacts. Far away from the contacts, C reaches its largest value when the nanowire is directly illuminated, as the contour plots perpendicular to the nanowire demonstrate. When the center of the laser spot is moved away from the nanowire along the horizontal direction, the voltage C drops to zero, because the topologically trivial silicon substrate does not generate spin-polarized currents. Non-zero values of C are only possible when the Bi_2Se_3 nanowire is illuminated. Therefore, spin-polarized currents are optically generated when the nanowire is illuminated. The impact of the gold contacts on the spin-polarized currents will be discussed in more detail in Sec. 1.6.

1.3.2 The thermoelectric current

All the effects discussed so far are based on optical transitions in the band structure. They depend on the optical selection rules and are thus represented by the polarization-dependent terms in Eq. (1.2). In addition to optical transitions, also thermoelectric effects contribute to the measured photocurrent, since the laser spot is smaller than the dimensions of the contact spacing for the nanowires and the Hall bar structure. The samples are heated unevenly along the lateral direction, which generates temperature gradients on the sample surface. This causes a thermovoltage based on the Seebeck effect which contributes to the polarization-independent parameter D in Eq. (1.2).
The Seebeck effect is named after Thomas Johann Seebeck based on his experiments in 1821 [49] and the additional explanation of Hans Christian Ørsted, who coined the term "thermoelectricity" [50]. Phenomenologically, the Seebeck effect describes the generation of a voltage difference ΔV across a conductor or semiconductor due to the diffusion of charge carriers along the temperature gradient $\Delta T = T_{\mathrm{hot}} - T_{\mathrm{cold}}$, since the mobility of the electrons at the heated position is higher than the mobility of the colder electrons. In the open-circuit condition, the charge carriers will accumulate in the cold region, resulting in the formation of an electric potential difference. The equilibrium state is reached when the charge movement is compensated by an internal electric field. The sign of the potential differs depending on whether electrons or holes are the majority charge carriers. The Seebeck coefficient S describes the magnitude of the Seebeck effect. For small temperature changes, it is given by [51, 52]

$$S = \frac{\Delta V}{\Delta T} \,. \tag{1.3}$$

The Seebeck coefficient of a specific material is usually determined by forming a thermocouple with a second material with a known Seebeck coefficient.
In the following, we consider a thermocouple, which consists of two materials A and B with different Seebeck coefficients S_{A} and S_{B} as in Fig. 1.8(a). The two materials are in electrical and thermal contact and a voltmeter is used to measure the thermovoltage. The temperature gradient is created by heating one junction. Specifically, the temperature T_2 of the second junction is higher than the temperature T_1 of the first junction. The voltmeter has a third temperature T_V. Applying Eq. (1.3) to the three sections of the

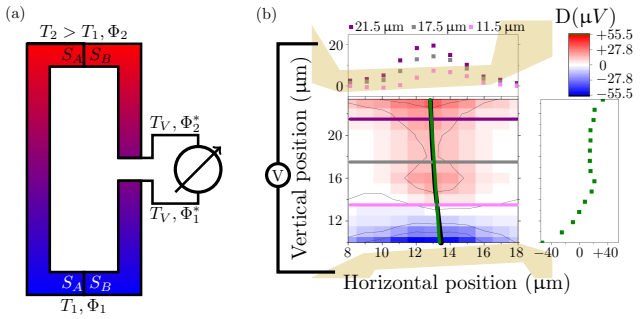

Figure 1.8: (a) Sketch of a thermocouple which mimics the device formed by the nanowire and the two contacts. (b) The map shows the parameter D which is related to the thermovoltage. The vertical contour plot in the right inset shows the parameter D along the nanowire and the horizontal contour perpendicular to the nanowire. The gold contacts are again marked by light orange shapes. The drain (source) electrode is at the top (bottom). Adapted from article I, sec 3.2.

closed circuit in Fig. 1.8(a), leads to

$$\begin{aligned} \Phi_2 - \Phi_2^* &= -S_\mathrm{B}\,(T_2 - T_V) \\ \Phi_2 - \Phi_1 &= -S_\mathrm{A}\,(T_2 - T_1) \\ \Phi_1^* - \Phi_1 &= -S_\mathrm{B}\,(T_V - T_1)\ , \end{aligned} \tag{1.4}$$

where Φ_i and Φ_j^* with $i, j = 1, 2$ are the potentials at positions indicated in Fig. 1.8(a). Based on Eq. (1.4), we get the net voltage

$$V = \Phi_2^* - \Phi_1^* = (S_\mathrm{B} - S_\mathrm{A})\,(T_2 - T_1) \tag{1.5}$$

detected by the voltmeter. In our measurement geometry for the nanowire devices, we expect that the thermovoltage contributes exclusively to the polarization-independent parameter D. For simplicity, we omit the 5 nm thick chromium interlayer and treat the contacts as a pure gold layer. The thermovoltage for the nanowire devices can then be written as

$$V = V_\mathrm{D} - V_\mathrm{S} = (S_\mathrm{Au} - S_\mathrm{TI})(T_\mathrm{D} - T_\mathrm{S})\ , \tag{1.6}$$

where S_Au is the Seebeck coefficient of the gold contact, S_TI is the nanowire Seebeck coefficient, T_D is the drain temperature (ground electrode), and T_S is the source temperature (minus pole). We have $S_\mathrm{Au} - S_\mathrm{TI} > 0$ in Eq. (1.6), since $S_\mathrm{Au} = 1.94\,\mu\mathrm{V/K}$ at 300 K and $S_\mathrm{TI} \approx -100\,\mu\mathrm{V/K}$ at 300 K [33]. When the drain electrode is illuminated, we get $T_\mathrm{D} > T_\mathrm{S}$ which results in a positive thermovoltage V according to Eq. (1.6). Illuminating the source electrode reverses the sign of the voltage.
In the following, we compare Eq. (1.6) with the spatial dependence of the parameter D. The experimental results for D are shown in Fig. 1.8(b). We observe that D changes its sign from positive at the top electrode (drain electrode) to negative at the lower electrode (source electrode). This is in good agreement with Eq. (1.6), as we now explain. Qualitatively, the laser light heats the sample locally. Hence, two temperature gradients with opposite signs are generated which point from the laser-spot position towards the two colder contacts. These temperature gradients add up to a net temperature gradient.

If the laser spot is closer to one contact than to the other one, the magnitude of the temperature gradients differ. Therefore, the position of the laser spot with respect to the contacts determines the magnitude of the net temperature gradient and the size and sign of the thermovoltage according to Eq. (1.6). When the laser spot is in the center between the contacts, the two temperature gradients cancel and the thermovoltage vanishes. The zero crossing occurs at the vertical position of 13 µm in Fig. 1.8(b) in the contour plot along the nanowire (green line).
The contour plots perpendicular to the nanowire (in purple, gray and pink) reveal that the highest values of D are reached when the center of the laser spot matches the horizontal position of the nanowire at 13 µm. If the laser spot is moved away from the nanowire along the horizontal direction, the values decrease. This means the silicon substrate does not contribute to the parameter D.
In summary, the polarization-independent parameter D results from the Seebeck effect. Possible contributions of the polarization-independent photon drag and photogalvanic effect appear to be negligible. Because of this, we assume that the direction and magnitude of the net temperature gradient at every laser spot position is encoded in the color map of D. By comparing the two-dimensional maps of C and D, we can connect the spin-polarized currents with the temperature distribution of the nanowire.
As before with C, we observe an enhancement of the thermovoltage D when the gold contacts and the nanowire underneath are illuminated. In our measurements, the enhancement appears at vertical positions above 21 µm and below 11 µm as shown in Fig. 1.8(b). Along the nanowire, the thermovoltage increases non-linearly in the vicinity of the contacts. This non-linearity cannot be explained by the Seebeck effect in Eq. (1.6), since the thermovoltage depends linearly on the temperature gradient. We relegate further discussion of the non-linear enhancement to Sec. 1.5.
The thermovoltage vanishes at a vertical position of 13 µm, which is 4 µm away from the center between the contacts. This shift was reproduced for multiple different nanowire samples and several measurements. We can exclude a misalignment of the laser beam as the reason for the shift, because the reflected intensity is invariant under a shift $\alpha \mapsto \alpha + 180°$ of the QWP. This means that the same polarization state is reached, as required for a properly aligned laser beam. In addition, we can exclude that the QWP is tilted with respect to the laser beam. In previous experiments, the QWP was tilted on purpose by less than 1° in such a way that the laser beam does not enter the QWP under an angle of 90°. This causes an additional motion of the laser spot on the sample surface, when rotating the QWP. As a result, the photocurrent contains an additional contribution with a period of 720°, since the Seebeck effect depends on the laser spot position. In the present experiments, we did not detect a contribution with this frequency and so we can exclude the QWP tilting as the reason for the shift.
A possible reason for the shift of the zero-crossing could be the asymmetrical heating of the laser beam. The Gaussian heat profile is not symmetrical at an angle of incidence of 45°. Another reason could be the enhancement of the thermovoltage at the Au/TI layer combined with the laser spot size. The FWHM of the laser spot in vertical direction is 2.86(6) µm. When the center of the laser is 3 µm away from the contacts, the Au/TI layer is still heated and contributes to the measured thermovoltage. In addition, the nanowire in this experiment is slightly bent as shown in Fig. 1.8(b) and the thermovoltage changes drastically when the laser spot is moved along the horizontal direction. Hence, the center

of the laser light does not always match the center of the nanowire when the laser spot is moved along the vertical direction, leading to small changes of the thermovoltage.

1.4 Photocurrent enhancement in the vicinity of the metallic contacts

In the previous section, the spin-polarized current and the thermovoltage were discussed in the area between the contacts via the two-dimensional maps for C and D. In both cases, we observed an enhancement of their values in the vicinity of the metal contacts. To show that this enhancement is not an artefact of a specific nanowire, we repeated the photocurrent measurements on a new set of nanowires. The measurements are performed under identical conditions as before with respect to the laser setup and the contact distance. However, some specific measurement settings are changed and the influence of different contact configurations is explored, to test the robustness of the enhancement. Our results are summarized in Figs. 1.9 and 1.10.
Fig. 1.9 shows the results for C and D on one of these new nanowires. In contrast to the nanowire used in the previous section, the new nanowire is oriented perpendicular to the oscillation plane of the excitation beam. In addition, the photocurrent is measured instead of the photovoltage. Inspite of these differences, the measured data is qualitatively in good agreement with the previous results in Fig. 1.7(d) and Fig. 1.8(b). In particular, we again observe the enhancement in the vicinity of the contacts. Specifically, the thermoelectric current reaches its extremal values of $D = -19.63(15)\,\mathrm{nA}$ and $D = 14.90(11)\,\mathrm{nA}$ at the crossing of the contact pads and the nanowire. In Fig. 1.9(c), the spin-polarized current reaches a maximum of $C = 0.34(9)\,\mathrm{nA}$ at the left side of the right-hand contact and a minimum of $C = -0.54(12)\,\mathrm{nA}$ at the right side of the right-hand contact. In contrast to the thermoelectric current, the spin-polarized current changes its sign at opposite sides of the same contact pad. We return to this point in Sec. 1.6.2.
Fig. 1.10 shows the results for the parameter D on a third nanowire for two different contact configurations, which we denote as axisymmetric and point symmetric. In both cases, the nanowire is oriented perpendicular to the oscillation plane of the excitation beam and the photovoltage is measured. The results for D are taken from two consecutive measurements of the same nanowire. The sample is kept in its holder and only the electrical connections to the sample holder are switched between the two measurements. For both contact geometries, we observe enhanced values at the crossing of the contacts and the nanowire, which is in good agreement with the previous results. Since the photovoltage is measured, the results for the thermovoltage can be compared quantitatively with Fig. 1.8(b). The thermovoltage in Fig. 1.10(a) reaches $D = 15.55(15)\,\mu\mathrm{V}$ at the drain electrode (left electrode) and goes down to $D = 1.11(10)\,\mu\mathrm{V}$ at position (12,9). These values are significantly smaller than in Fig. 1.8(b). One reason for this decrease is the different orientation of the oscillation plane of the excitation beam. This changes the amount of laser light absorbed by the sample, since the absorption rate for s- and p-polarized light is different (In our case, the nanowire is rotated instead of the oscillation plane, but the result remains the same.). The main reason for the smaller values of D can be attributed to a poorer quality of the bond pads in Fig. 1.10. Here,

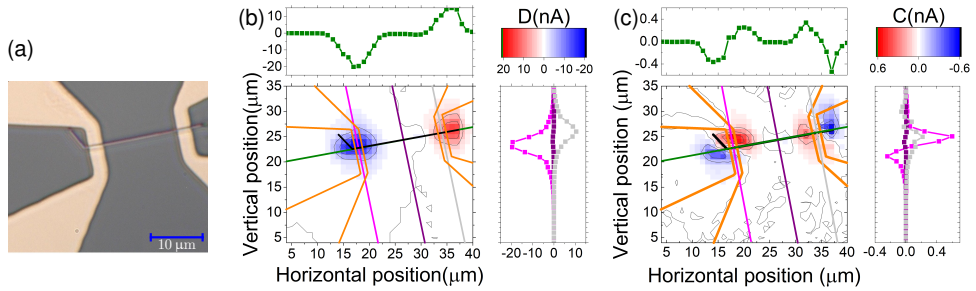

Figure 1.9: Photocurrent measurement on a Bi_2Se_3 nanowire with a 14 µm gap with the drain (source) electrode on the right (left). (a) The micrograph of the measured area. (b, c) Spatially resolved results for the thermoelectric current D and the spin-polarized current C, including contour plots along the nanowire (green lines), the contacts (pink and gray lines) and through the center of the nanowire (violet lines). Adapted from article II, sec 3.3.

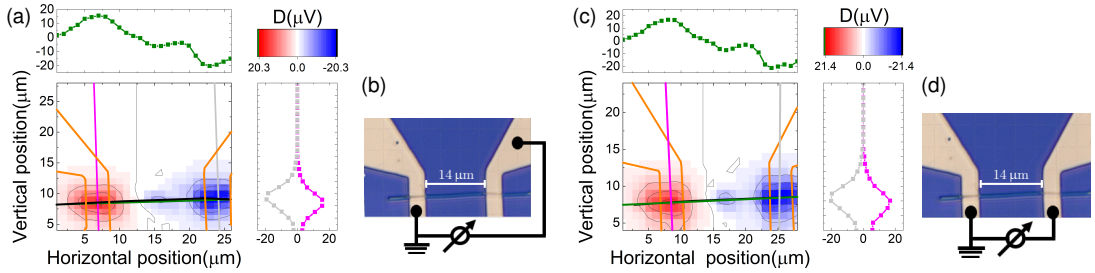

Figure 1.10: Thermovoltage D measurements on a Bi_2Se_3 nanowire for different contacts. (a) Thermovoltage D for the axisymmetric bonding. (b) The axisymmetric bonding is marked in black on a micrograph of the sample. (c) Thermovoltage D for the point-symmetric bonding. (d) Sketch of the point-symmetric bonding is displayed. The contour plots in (a) and (c) along the nanowire (green lines) and along the contacts (pink and gray lines) are displayed next to the maps. Adapted from article II, sec 3.3.

the contact pads are not in good contact with the substrate and the nanowire, leading to a decrease in the amount of electrons transitioning from the nanowire into the metal contact.
Inspite of this, the characteristic features - the sign change and the enhancement of the thermovoltage close to the metal contacts - are visible for both contact geometries. This proves that different contact configurations do not influence the thermovoltage as Fig. 1.10(a) and (c) give nearly identical results.

1.5 The Schottky effect and the thermoelectric current

Having established the robustness of the enhancement at the metallic contacts, we now discuss its origin for the thermovoltage D. The mechanism which is responsible for the enhancement of the spin-polarized current C will be discussed later in Sec. 1.6. The band gap of Bi_2Se_3 is 300 meV [11] which is in the range of a semiconductor band gap. At the interface between the nanowire and the metallic contact, band bending occurs

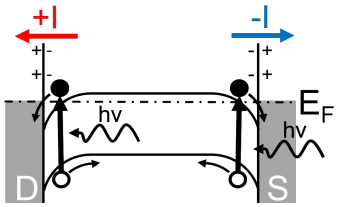

Figure 1.11: Illustration of the band bending at the contact/nanowire/contact interfaces. Adapted from article II, sec 3.3.

similar to the scheme in Fig. 1.11 to compensate the different work functions of the Bi_2Se_3 nanowire and the metal contact. Due to the band bending, a positive (negative) space-charge region forms in the contact (nanowire) close to the interface at the drain electrode.
When the laser illuminates the nanowire underneath the drain electrode, an electron-hole pair is created. The electron will be accelerated to the drain electrode and the hole to the center of the nanowire, driven by the electric field around the interface. The electrons entering the drain electrode will contribute to a net-positive current while the holes annihilate with electrons originating from the source electrode. The photoelectrons generated close to the source electrode contribute to a net-negative current, since the electric field of the space-charge region changes its sign.
The enhancement at the drain electrode has a maximum at position (7,7) and decreases when the laser spot is moved away from there. The decrease is due to the Gaussian laser intensity profile. When the laser spot is moved away from position (7,7), less photons illuminate the interface of the nanowire and the metal contact and the current decreases. The same effect appears at the source electrode but with an opposite sign. To summarize, the enhancement of the thermovoltage at the interface between the nanowire and the metallic contacts arises due to the Schottky effect.
This explanation is in good agreement with photovoltage measurements on ZnO and Si semiconductor nanowires contacted by metallic contact pads [53, 54]. Park et al. and Ahn et al. both also observe an enhancement of the photocurrent at the interface between the topologically-trivial semiconductor nanowire and the metallic contact when illuminated, which agrees qualitatively with the results for the topologically non-trivial Bi_2Se_3 nanowires discussed in this thesis.
We exclude a second explanation for the enhancement discussed by Leonard et al., who performed spatially-resolved optoelectronic measurements on GaN/AlGaN core shell nanowires and observed a similar enhancement of the photovoltage at the interface [55]. They ruled out the Schottky effect, since their contacts show an ohmic behavior and the metal contacts absorb most of the laser light before it reaches the nanowire underneath the contact. Hence, no electron-hole pairs are created at the interface between the metal contact and the nanowire. Instead, they model the metal contacts on top of the nanowire as a thin film with a heat transfer at the bottom. They estimate that the heat dissipation takes roughly 5 ns, which is too fast for the measurement technique used in this thesis. Hence, we rule out the heat transfer from the metal contact through the nanowire as the origin of the enhaced values.

1.6 The spin Nernst effect and the spin-polarized current

Up to now, we have treated the thermoelectric current D and the spin-polarized current C as independent quantities. However, an inhomogeneous temperature distribution can generate additional spin-polarized currents via the spin Nernst effect. In the following, we investigate this correlation between C and D for the $(Bi_{0.57}Sb_{0.43})_2\,Te_3$ thin film Hall bar structures in Sec. 1.6.1 and for the Bi_2Se_3 nanowires in Sec. 1.6.2.

1.6.1 Hall bar devices

The typical geometry of the Hall bar devices is displayed as a microscope image in Fig. 1.12(a). In this image, three areas can be distinguished: The Hall bar, colored in light gray, is the three-dimensional topological insulator, the yellow areas are the gold contacts and the dark gray areas are Si (111), i.e. the uppermost layer of the substrate. The topological material for the Hall bar structure is $(Bi_{0.57}Sb_{0.43})_2\,Te_3$, a ternary layer structure with a total thickness of 16 nm. The sample is bonded in the same manner as the nanowire samples in the previous sections. The laser settings ($\lambda = 785\,\text{nm}$, $f = 77\,\text{Hz}$) and the spot size (FWHM $\approx 3\,\mu\text{m}$) of the photocurrent measurements are also identical. The distance between the two contacts marked on the microscope image in Fig. 1.12(a) is 150 µm, which is roughly one order of magnitude larger than the contact spacing of the nanowire samples.
The measurement on the Hall bar device is carried out as described in Sec. 1.2 with a step size of 10 µm in the vertical and horizontal direction. The measured reflected intensity in Fig. 1.12(b) is again used to determine the position of the topological insulator Hall bar (dark gray area), the beginning of the four gold contacts on top of the Hall bar (white areas), and the silicon substrate (black areas).
The thermovoltage is displayed in Fig. 1.12(c). The sign of the thermovoltage changes when the laser spot is moved from the first electrode to the second electrode. This is in good agreement with the Seebeck effect and the nanowire measurements in Fig. 1.8(b). The contour plot in the vertical direction along the Hall bar (black line) clearly shows the linear functional dependence of the thermovoltage until the laser spot reaches the vicinity of the crossing of the Hall bar. Here, the large values at the edges of the triangular-shaped ends contribute, since the contour plot averages over the total width (20 µm) of the Hall bar. In the horizontal direction (gray line), the thermovoltage D reaches the largest values around 0.3 mV and drops down to zero when the substrate is illuminated. The thermovoltage also drops to zero at the overlap of the gold contacts and the TI, in direct contrast to the enhancement observed for the nanowire samples. The contact layer is probably too thick, so the laser light is mostly absorbed in the metal layer before generating electron-hole pairs at the contact/topological insulator interface. As a result, the Schottky effect can not occur here.
The measured values for C in Fig. 1.12(d) are in the range of $-4\,\mu\text{V}$ to $+4\,\mu\text{V}$ which is two orders of magnitude smaller than the thermovoltage. Along the horizontal direction (gray line), the values fluctuate around zero. The color map does not show any organized structure and the values of C for the substrate and the Hall bar are indistinguishable. Based on this data, it is not clear if a spin-polarized current is generated in the Hall bar device.

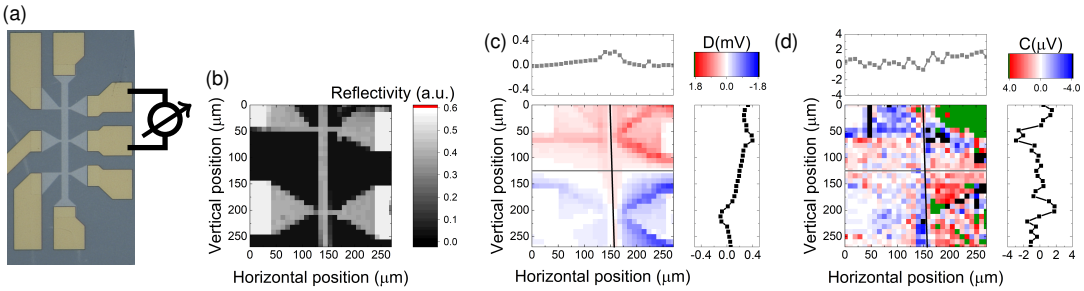

Figure 1.12: Results for photocurrent measurements with a coarse scanning grid on a Hall bar. (a) Microscope image of the sample. The bonds are marked in black. (b) Intensity of the reflected laser light. The gold contacts (white), the Si substrate (black), and the topological insulator (gray) can be clearly distinguished. (c,d) Two-dimensional maps of the thermovoltage D and the voltage C induced by the spin-polarized current. For both parameters, contour plots along (black) and perpendicular to (gray) the Hall bar are shown. Adapted from article III, sec 3.4.

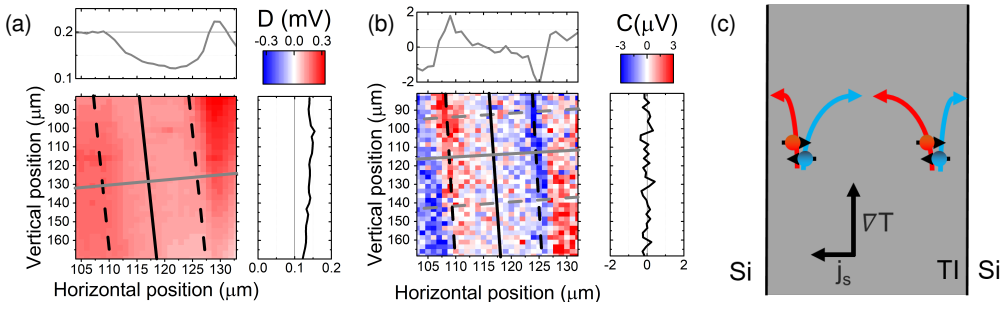

Figure 1.13: Results for photocurrent measurements with a fine scanning grid on a Hall bar. (a, b) Two-dimensional map of the thermovoltage D and the voltage C induced by the spin-polarized current. The contour plots along the Hall bar (black line) are averaged over its total width of 20 µm. The contour plots perpendicular to the topological insulator (TI) Hall bar (gray line) are averaged over 50 µm. (c) Spin accumulation at the Hall bar edges due the spin-dependent deflection of the electrons via the spin Nernst effect. (a, b) Adapted from article III, sec 3.4.

To investigate whether a spin-polarized current can be generated in the Hall bar devices, the photocurrent measurements are repeated using a finer grid with a step size of 1 µm in the horizontal and 2 µm in the vertical direction. The result for C and D are shown in Fig. 1.13 (a) and (b). The thermovoltage decreases linearly from the top to the bottom of the Hall bar, as shown in the vertical contour plot. This is in good agreement with the results for the coarser grid in Fig. 1.12(c). Along the Hall bar, the voltage C fluctuates between $-0.5\,\mu V$ and $+0.5\,\mu V$. Hence, no spin-polarized current is generated in the Hall bar center. Closer to its edges, which are marked by black stripes in Fig. 1.13(b), C reaches positive values at the left edge and negative values at the right edge. The contour plot along the horizontal direction averaged over 50 µm reveals that C reaches up to $+1.9\,\mu V$ at the left and down to $-2\,\mu V$ at the right edge. This result is surprising, since we would expect that C has the same sign across the entire Hall bar.
The sign conversion of C at the two edges can be explained by the spin Nernst effect, which describes the spin separation caused by a thermal flow of electrons. This generates

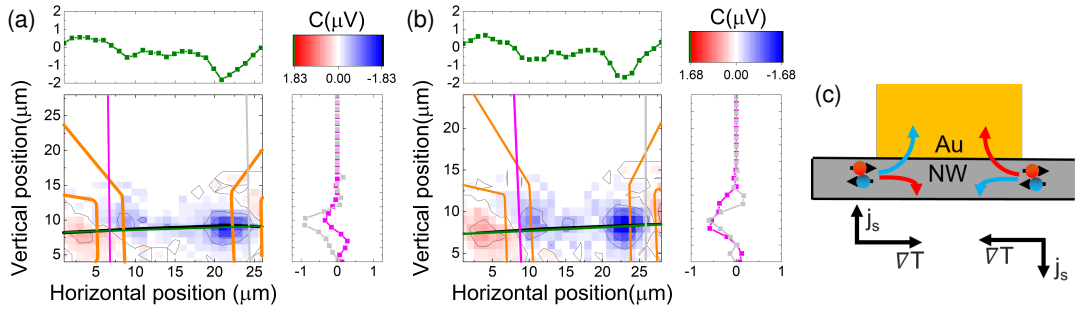

Figure 1.14: Voltage C on a Bi_2Se_3 nanowire for different contacts. (a) and (b) show maps of the voltage C for axi- and point-symmetric configurations, respectively. The contour plots along the nanowire (green lines) and along the contacts (pink and gray lines) are displayed next to the maps. (c) Spin accumulation at the drain electrode due the spin-dependent deflection of the electrons via the spin Nernst effect. The sketch provides a side view of the interface, with the gold contacts (Au) sitting on top of the nanowire (NW). Adapted from article II, sec 3.3.

a transverse spin current j_s which is driven by a temperature gradient ∇T. Specifically, the spin-up and spin-down electrons are deflected perpendicular to the temperature gradient in opposite directions. This leads to a transverse spin current [56]. From the vertical contour plot of Fig. 1.13(a), we can deduce that a temperature gradient parallel to the Hall bar exists and so electrons with opposite spin are deflected towards opposite Hall bar edges via the spin Nernst effect. For concreteness, let us assume that spin-down (spin-up) electrons are deflected towards the left (right) edge. Then more spin-down electrons populate the surface states than spin-up electrons at the left edge. This causes an asymmetric population of the surface states at the left edge. At the right edge, the opposite is true, leading to a mirrored asymmetric population of the surface states, see Fig. 1.13(c). Consequently, spin-polarized currents of opposite signs emerge at the two edges, which explains our experimental results.

1.6.2 Nanowires

We can not observe the exact same effect on the nanowire due to its comparatively smaller width with respect to the 3 µm laser-spot size. Hence, it is not possible to illuminate the opposite sides of the nanowire separately. Thus, no spin accumulation can be detected at opposite sides of the nanowire. However, the spin Nernst effect provides an explanation for the enhanced values of C in the vicinity of the metallic contacts. In particular, the sign change of C at opposite sides of the same contact pad can be explained with the spin Nernst effect. This sign change was first observed in Fig. 1.9(c) and is reproduced in Fig. 1.14(a) and (b) for the nanowire with axisymmetric and point-symmetric contacts. Qualitatively, the distribution of the C values stays the same for the two contact geometries. Hence, fluctuations of the spin-polarized current as in ref. [27] can not cause the enhancement in our measurements.
The sign conversion at the two sides of each contact bear close resemblance to the spin accumulation at the Hall bar edges discussed above. During the analysis of the thermovoltage at the metal contacts in Sec. 1.4, we already discussed that a temperature

gradient exists, which decreases radially from the center of the contact, see Fig 1.10. Hence, the temperature gradient has a component pointing along the nanowire. As shown for the drain electrode (left electrode) in Fig. 1.14(c), the direction of the temperature gradient ∇T is different for the two contact edges. Because of the spin Nernst effect, electrons with opposite spin orientations are deflected perpendicular to the temperature gradient ∇T in opposite directions, which generates a spin current j_s. When the laser spot illuminates the left edge, the spin-up electrons (depicted in blue) are deflected towards the interface and can enter the gold layer. Hence, the population of the Dirac cone is asymmetric. At the right edge, the temperature gradient ∇T points in the opposite direction. Thus, the spin-down electrons (depicted in red) are deflected into the gold layer. This means more surface states are populated by spin-up than spin-down electrons. Thus, the spin-polarized currents at the two edges of the drain electrode have opposite sign, leading to a sign change of C from positive at the left edge to negative at the right edge. Analogous results follow for the source electrode (right electrode), with inverted roles for its left and right edge since the sign of the temperature gradient is reversed.

1.7 Conclusion and outlook

In this thesis, we performed photocurrent measurements on the surface of three-dimensional topological insulators. Specifically, the nanowires are made of Bi_2Se_3 and the Hall bars consist of $(Bi_{0.57}Sb_{0.43})_2\,Te_3$. We focused on the spatial distribution of the photocurrent and its dependence on the polarization of the excitation light. From these measurements, we obtained two-dimensional maps of the polarization-independent and helicity-dependent components of the photocurrents.
We find that the polarization-independent component D is dominated by the Seebeck effect and thus driven by thermoelectric currents. Potential contributions from the polarization-independent photogalvanic and photon drag effect are negligible. The helicity-dependent component C, on the other hand, is driven by the spin-polarized currents that emerge from the topologically non-trivial helical surface states via the CPGE.
First and foremost, our experiments demonstrate that topological insulator nanowires provide a promising platform for the generation of spin-polarized currents, whose direction can be controlled via the helicity of the excitation light. They also highlight the importance of analyzing the spatial distribution of the photocurrent, as we observe a strong enhancement of the spin-polarized current C and the thermoelectric current D at the interface between the nanowire and the metallic contacts.
As our analysis shows, the Schottky effect enhances the thermoelectric current at the contacts. The enhancement of the spin-polarized current C is correlated with D. For the nanowires, a temperature gradient from the nanowire into the contacts is observed in the distribution of the thermoelectric current. This temperature gradient in turn generates spin-polarized currents via the spin Nernst effect which are the reason for the enhancement of C at the contacts. We observe a similar effect at the edges of the Hall bar devices, where spin accumulation is again driven by a temperature gradient along the topological insulator and thus the spin Nernst effect.

To further investigate the increase of the spin-polarized current at the contacts, it would be interesting to change the sample design. For example, measuring the spin-polarized current of a nanowire device with broader metal contacts, which also cover the end of the nanowire. This would allow us to identify whether the nanowire end, the contact edge, or the nanowire underneath the metal contact causes the enhancement of the spin-polarized current.
In this thesis, the composition of the nanowires is the same for all samples. By changing the composition and thus the doping of the topological insulator nanowire the bulk-carrier conduction can be further suppressed relative to the surface conduction. This would increase the magnitude of the spin-polarized current C compared to the other photocurrent contributions. Large values of C compared to the other photocurrent contributions are an essential requirement for any potential applications of topological insulators in the field of spintronics.
Beyond the present experimental setup, our experimental technique is a suitable tool to measure two-dimensional current maps of a combination of two or more topological insulator nanowires, which are arranged crosswise. Such samples could, e.g., be built from nanoribbons which have recently been successfully fabricated by Rosenbach et al. [57]. These nanoribbons, in contrast to the nanowires in this thesis, yield the advantage of controlling the nanoribbon placement on the substrate. Crossed nanowires and nanoribbons could be used to generate circular-polarized THz radiation. If the correct excitation frequency is used, each nanowire should emit linear-polarized THz radiation like Seifert et al. [58] reported for Bi_2Te_2Se nanowires. Consequently, circular polarized THz radiation is generated through interference, since the two nanowires are arranged perpendicular to each other.

2 Bibliography

[1] C. L. Kane and E. J. Mele, Phys. Rev. Lett. **95**, 146802 (2005).

[2] C. L. Kane and E. J. Mele, Phys. Rev. Lett. **95**, 226801 (2005).

[3] M. Z. Hasan and C. L. Kane, Rev. Mod. Phys. **82**, 3045 (2010).

[4] L. Isaev, Y. H. Moon, and G. Ortiz, Phys. Rev. B **84**, 075444 (2011).

[5] C.-K. Chiu, J. C. Y. Teo, A. P. Schnyder, and S. Ryu, Rev. Mod. Phys. **88**, 035005 (2016).

[6] L. Fu, C. L. Kane, and E. J. Mele, Phys. Rev. Lett. **98**, 106803 (2007).

[7] J. E. Moore and L. Balents, Phys. Rev. B **75**, 121306 (2007).

[8] R. Roy, Phys. Rev. B **79**, 195322 (2009).

[9] D. Hsieh, D. Qian, L. Wray, Y. Xia, Y. S. Hor, R. J. Cava, and M. Z. Hasan, Nature **452**, 970 (2008).

[10] H. Zhang, C.-X. Liu, X.-L. Qi, X. Dai, Z. Fang, and S.-C. Zhang, Nature Physics **5**, 438 (2009).

[11] Y. Xia, D. Qian, D. Hsieh, L. Wray, A. Pal, H. Lin, A. Bansil, D. Grauer, Y. S. Hor, R. J. Cava, and M. Z. Hasan, Nature Physics **5**, 398 (2009).

[12] T. Zhang, P. Cheng, X. Chen, J.-F. Jia, X. Ma, K. He, L. Wang, H. Zhang, X. Dai, Z. Fang, X. Xie, and Q.-K. Xue, Phys. Rev. Lett. **103**, 266803 (2009).

[13] Z. Alpichshev, J. G. Analytis, J.-H. Chu, I. R. Fisher, Y. L. Chen, Z. X. Shen, A. Fang, and A. Kapitulnik, Phys. Rev. Lett. **104**, 016401 (2010).

[14] M. Romanowich, M.-S. Lee, D.-Y. Chung, S. D. Mahanti, M. G. Kanatzidis, and S. H. Tessmer, Phys. Rev. B **87**, 085310 (2013).

[15] D. Hsieh, Y. Xia, D. Qian, L. Wray, J. H. Dil, F. Meier, J. Osterwalder, L. Patthey, J. G. Checkelsky, N. P. Ong, A. V. Fedorov, H. Lin, A. Bansil, D. Grauer, Y. S. Hor, R. J. Cava, and M. Z. Hasan, Nature **460**, 1101 (2009).

[16] Y. L. Chen, J. G. Analytis, J.-H. Chu, Z. K. Liu, S.-K. Mo, X. L. Qi, H. J. Zhang, D. H. Lu, X. Dai, Z. Fang, S. C. Zhang, I. R. Fisher, Z. Hussain, and Z.-X. Shen, Science **325**, 178 (2009).

[17] L. Plucinski, G. Mussler, J. Krumrain, A. Herdt, S. Suga, D. Grützmacher, and C. M. Schneider, Applied Physics Letters **98**, 222503 (2011).

[18] Y. H. Wang, D. Hsieh, D. Pilon, L. Fu, D. R. Gardner, Y. S. Lee, and N. Gedik, Phys. Rev. Lett. **107**, 207602 (2011).

[19] F. Boschini, M. Mansurova, G. Mussler, J. Kampmeier, D. Grützmacher, L. Braun, F. Katmis, J. S. Moodera, C. Dallera, E. Carpene, C. Franz, M. Czerner, C. Heiliger, T. Kampfrath, and M. Münzenberg, Scientific Reports **5**, 15304 (2015).

[20] M. C. Wang, S. Qiao, Z. Jiang, S. N. Luo, and J. Qi, Phys. Rev. Lett. **116**, 036601 (2016).

[21] J. W. McIver, D. Hsieh, H. Steinberg, P. Jarillo-Herrero, and N. Gedik, Nature Nanotechnology **7**, 96 (2012).

[22] E. L. Ivchenko and G. E. Pikus, JETP Lett. **27**, 604 (1978).

[23] V. Belinicher, Physics Letters A **66**, 213 (1978).

[24] S. D. Ganichev, H. Ketterl, W. Prettl, E. L. Ivchenko, and L. E. Vorobjev, Applied Physics Letters **77**, 3146 (2000).

[25] S. D. Ganichev and W. Prettl, Journal of Physics: Condensed Matter **15**, R935 (2003).

[26] F. Meier and B. Zakharchenya, *Optical Orientation*, 1st ed., Vol. 8 (Elsevier, 1984).

[27] C. Kastl, C. Karnetzky, H. Karl, and A. W. Holleitner, Nature Communications **6**, 6617 (2015).

[28] K. N. Okada, N. Ogawa, R. Yoshimi, A. Tsukazaki, K. S. Takahashi, M. Kawasaki, and Y. Tokura, Phys. Rev. B **93**, 081403 (2016).

[29] H. Plank, S. N. Danilov, V. V. Bel'kov, V. A. Shalygin, J. Kampmeier, M. Lanius, G. Mussler, D. Grützmacher, and S. D. Ganichev, Journal of Applied Physics **120**, 165301 (2016).

[30] L. Braun, G. Mussler, A. Hruban, M. Konczykowski, T. Schumann, M. Wolf, M. Münzenberg, L. Perfetti, and T. Kampfrath, Nature Communications **7**, 2041 (2016).

[31] S. Luo, L. He, and M. Li, Nature Communications **8**, 2141 (2017).

[32] B. Hamdou, J. Kimling, A. Dorn, E. Pippel, R. Rostek, P. Woias, and K. Nielsch, Advanced Materials **25**, 239 (2013).

[33] H. S. Shin, B. Hamdou, H. Reith, H. Osterhage, J. Gooth, C. Damm, B. Rellinghaus, E. Pippel, and K. Nielsch, Nanoscale **8**, 13552 (2016).

[34] C. Weyrich, M. Drögeler, J. Kampmeier, M. Eschbach, G. Mussler, T. Merzenich, T. Stoica, I. E. Batov, J. Schubert, L. Plucinski, B. Beschoten, C. M. Schneider, C. Stampfer, D. Grützmacher, and T. Schäpers, Journal of Physics: Condensed Matter **28**, 495501 (2016).

[35] J. Kellner, M. Eschbach, J. Kampmeier, M. Lanius, E. Młyńczak, G. Mussler, B. Holländer, L. Plucinski, M. Liebmann, D. Grützmacher, C. M. Schneider, and M. Morgenstern, Applied Physics Letters **107**, 251603 (2015).

[36] J. Krumrain, G. Mussler, S. Borisova, T. Stoica, L. Plucinski, C. Schneider, and D. Grützmacher, Journal of Crystal Growth **324**, 115 (2011).

[37] G. Mussler, physica status solidi (b) **258**, 2000007 (2021).

[38] J. A. Arnaud, W. M. Hubbard, G. D. Mandeville, B. de la Clavière, E. A. Franke, and J. M. Franke, Appl. Opt. **10**, 2775 (1971).

[39] S. Ganichev and W. Prettl, *Intense Terahertz Excitation of Semiconductors* (Oxford University Press, 2006).

[40] M. V. Durnev and S. A. Tarasenko, Annalen der Physik **531**, 1800418 (2019).

[41] E. L. Ivchenko and S. D. Ganichev, (2017), arXiv:1710.09223 [cond-mat.mes-hall] .

[42] V. A. Shalygin, H. Diehl, C. Hoffmann, S. N. Danilov, T. Herrle, S. A. Tarasenko, D. Schuh, C. Gerl, W. Wegscheider, W. Prettl, and S. D. Ganichev, JETP Letters **84**, 570 (2007).

[43] P. Olbrich, L. E. Golub, T. Herrmann, S. N. Danilov, H. Plank, V. V. Bel'kov, G. Mussler, C. Weyrich, C. M. Schneider, J. Kampmeier, D. Grützmacher, L. Plucinski, M. Eschbach, and S. D. Ganichev, Phys. Rev. Lett. **113**, 096601 (2014).

[44] H. Plank, L. E. Golub, S. Bauer, V. V. Bel'kov, T. Herrmann, P. Olbrich, M. Eschbach, L. Plucinski, C. M. Schneider, J. Kampmeier, M. Lanius, G. Mussler, D. Grützmacher, and S. D. Ganichev, Phys. Rev. B **93**, 125434 (2016).

[45] G. M. Mikheev, A. S. Saushin, V. M. Styapshin, and Y. P. Svirko, Scientific Reports **8**, 8644 (2018).

[46] V. A. Shalygin, M. D. Moldavskaya, S. N. Danilov, I. I. Farbshtein, and L. E. Golub, Phys. Rev. B **93**, 045207 (2016).

[47] L. Zhu, Z. Yao, Y. Huang, C. He, B. Quan, J. Li, C. Gu, X. Xu, and Z. Ren, Phys. Rev. Applied **12**, 044063 (2019).

[48] Y. Zhang, K. He, C.-Z. Chang, C.-L. Song, L.-L. Wang, X. Chen, J.-F. Jia, Z. Fang, X. Dai, W.-Y. Shan, S.-Q. Shen, Q. Niu, X.-L. Qi, S.-C. Zhang, X.-C. Ma, and Q.-K. Xue, Nature Physics **6**, 584 (2010).

[49] T. J. Seebeck, Abhandlungen der Königlich Preußischen Akademie der Wissenschaften zu Berlin , 265 (1822).

[50] H. C. Oersted, Annalen der Physik **73**, 430 (1823).

[51] C. C. Sorrell, S. Sugihara, and J. Nowotny, eds., *Materials for Energy Conversion Devices*, Woodhead Publishing Series in Electronic and Optical Materials (Woodhead Publishing, 2005).

[52] O. Ostroverkhova, ed., *Handbook of Organic Materials for Electronic and Photonic Devices*, second edition ed., Woodhead Publishing Series in Electronic and Optical Materials (Woodhead Publishing, 2019).

[53] C. Park, J. Lee, H.-M. So, and W. S. Chang, J. Mater. Chem. C **3**, 2737 (2015).

[54] Y. Ahn, J. Dunning, and J. Park, Nano Letters **5**, 1367 (2005).

[55] F. Léonard, E. Song, Q. Li, B. Swartzentruber, J. A. Martinez, and G. T. Wang, Nano Letters **15**, 8129 (2015).

[56] S. Meyer, Y.-T. Chen, S. Wimmer, M. Althammer, T. Wimmer, R. Schlitz, S. GeprAgs, H. Huebl, D. Kadderitzsch, H. Ebert, G. E. W. Bauer, R. Gross, and S. T. B. Goennenwein, Nature Materials **16**, 977 (2017).

[57] D. Rosenbach, N. Oellers, A. R. Jalil, M. Mikulics, J. Kölzer, E. Zimmermann, G. Mussler, S. Bunte, D. Grützmacher, H. Lüth, and T. Schäpers, Advanced Electronic Materials **6**, 2000205 (2020).

[58] P. Seifert, K. Vaklinova, K. Kern, M. Burghard, and A. Holleitner, Nano Letters **17**, 973 (2017).

3 Cumulative thesis articles

3.1 Author contributions

Article I: Photocurrent measurements on topological insulator Bi_2Se_3 nanowires
N. Meyer, K. Geishendorf, J. Walowski, A. Thomas and M. Münzenberg, *Appl. Phys. Lett.* 116, 172402 (2020)
N.M. performed the experiment and data analysis. K.G. synthesized the nanowires. N.M wrote the manuscript, which was edited by all authors.

Article II: The impact of metallic contacts on spin-polarized photocurrents in topological insulator Bi_2Se_3 nanowires
N. Meyer, K. Geishendorf, J. Walowski, A. Thomas and M. Münzenberg, *Appl. Phys. Lett.* 117, 262401 (2020)
N.M. performed the experiment and data analysis. K.G. synthesized the nanowires. N.M wrote the manuscript, which was edited by all authors.

Article III: Observation of spin Nernst photocurrents in topological insulators
T. Schumann, N. Meyer, G. Mussler, J. Kampmeier, D. Grützmacher, E. Schmoranzerová, L. Braun, T. Kampfrath, J. Walowski, M. Münzenberg (submitted)
M.M. and E.S. designed the experiment. T.S., N.M., J.W., E.S., developed the interfaces to measure and analyze the experimental data and carried out the photocurrent experiments. M.M., T.S., J.W. and E.S. developed the model. G.M., J.K., and D.G. prepared and characterized the samples. T.S., N.M., G.M., J.K., D.G., L.B., T.K., J.W. and M.M. discussed the data and interpretation. T.S., E.S., G.M., J.W. and M.M wrote the manuscript. All the authors reviewed and discussed the manuscript.

Confirmed:

Greifswald, den Nina Meyer Markus Münzenberg

3.2 Photocurrent measurements on topological insulator Bi_2Se_3 nanowires

Applied Physics Letters ARTICLE scitation.org/journal/apl

Photocurrent measurements in topological insulator Bi_2Se_3 nanowires

Cite as: Appl. Phys. Lett. **116**, 172402 (2020); doi: 10.1063/1.5142837
Submitted: 18 December 2019 · Accepted: 14 April 2020 ·
Published Online: 27 April 2020

N. Meyer,[1,a)] K. Geishendorf,[2] J. Walowski,[1] A. Thomas,[2] and M. Münzenberg[1]

AFFILIATIONS

[1]Institute of Physics, University of Greifswald, Felix-Hausdorff-Str. 6, 17489 Greifswald, Germany
[2]IFW Dresden, Institute for Metallic Materials, Helmholtzstraße 20, 01069 Dresden, Germany

[a)]Author to whom correspondence should be addressed: nina.meyer@uni-greifswald.de

ABSTRACT

Circular photogalvanic currents are a promising approach for spin-optoelectronics. To date, such currents have been induced in topological insulator flakes or extended films. It is not clear whether they can be generated in nanodevices. In this paper, we demonstrate the generation of circular photogalvanic currents in Bi_2Se_3 nanowires. Each nanowire shows topological surface states. Here, we generate and distinguish the different photocurrent contributions via the driving light wave. We separate the circular photogalvanic currents from those due to thermal Seebeck effects through controlling laser light polarization. The results reveal a spin-polarized surface-Dirac electron flow in the nanowires arising from spin-momentum locking and spin–orbit effects. The second photocurrent contribution described in this Letter is caused by the thermal Seebeck effect. By scanning the photocurrent, it can be spatially resolved; upon reversing the gradient direction along the nanowire, the photocurrent changes its sign, and close to the gold contacts, the amplitudes of the different photocurrent contributions are affected by the proximity to the contacts. In the center of the nanowires, where the effects from the gold contact/topological insulator stacks vanish, the spin-polarized current remains constant along the nanowires. This allows the all-optical spin current generation in topological insulator nanowires and hybrid structures on the nanoscale, one goal of spin-orbitronics.

In the last decade, a class of topological matter, the so-called quantum spin Hall (QSH) insulators or topological insulators (TIs), theoretically predicted in 2005 by Kane and Mele and realized in two-dimensional (2D) in 2007 by König *et al.* in CdTe/HgTe quantum wells,[1,2] has attracted great attention. This class of matter has the interesting property of an energy gap between the valence and conduction bands that are closed at the boundaries by gapless surface states with high mobility and strong spin polarization.[3] The surface states are predicted to be topologically protected since their origin lies in intrinsic bulk properties such as large spin–orbit coupling, opposite parity of the bulk bands, band inversion, and time-reversal symmetry, which suppress backscattering and thereby decrease the sensitivity to surface impurities or defects. Additionally, the direction of the spin and momentum for the surface states are locked, giving rise to a strong spin polarization that makes these materials very interesting for spintronic applications, e.g., as spin injectors.[4]

After the realization of a 1D topologically nontrivial edge state, 3D topological insulators consisting of $Bi_{1-x}Sb_x$, Bi_2Se_3, Bi_2Te_3, and Sb_2Te_3 were also realized.[5,6] Over the last decade, the electronic properties of Bi_2Se_3 and Bi_2Te_3 have been extensively studied, with optimization of the properties of their topologically protected surface states. This has been carried out mainly by investigating the band structure of the surface electrons by imaging the band structure using angle resolved photoemission spectroscopy (ARPES),[7,8] including the spin-resolved variant, and time-resolved two-photon photoelectron (2PPE) spectroscopy.[9] Scanning tunneling microscopy (STM) can also be used to prove the existence of a linear dispersion relation and suppressed backscattering.[10]

To make use of these surface states in spintronics, it is essential not only to demonstrate the existence of spin-polarized surface states but also to control them. One approach for controlling these surface states is to create an asymmetrically populated Dirac cone, which leads to spin-polarized currents on the surface due to spin-momentum locking. This idea has been realized among others for exfoliated Bi_2Se_3[11] and other materials and is enabled by strong spin–orbit coupling in topological insulators such as Bi_2Se_3, lifting the spin degeneracy of the electrons in the surface states. As a result, the selection rules for interband transitions depend on the electron spin. Therefore, it is possible to use circular polarized light to selectively excite surface electrons with a parallel or antiparallel spin component with respect to the

photon momentum and depending on helicity. This creates an asymmetric population of surface states in k-space, which, due to the spin-momentum locking, leads to a spin-polarized electrical current [see Fig. 1(a)]. This effect of generating a spin-polarized charge current by creating an asymmetric carrier population in k-space by exciting optical transitions with circular polarized light imposed by optical selection rules is referred to as the circular photogalvanic effect (CPGE) and has been previously realized in semiconductor quantum wells.[12]

More recently, several studies have performed photocurrent measurements of the $Bi_{1-x}Sb_x$, Bi_2Se_3, Bi_2Te_3, and Sb_2Te_3 group using photon wavelengths ranging from the visible to the terahertz to the infrared regime.[13–17] In this work, we demonstrate spin-polarized photogalvanic effects in Bi_2Se_3 nanowires with a cross section in the nanometer range instead of micrometer-wide Hall bar structures used in previous experiments.[11,18] From a geometrical point of view, the ratio of surface to bulk states in nanowires should be higher due to their more rectangular cross section, which might lead to an increased ratio of spin-polarized currents to photocurrents originating from the bulk states.

Bi_2Se_3 nanowires were synthesized by the Au-catalyzed vapor–liquid–solid method on a Si(111) substrate (as described in Ref. 19). The cross section of the nanowires is either rectangular or trapezoidal, resulting from the layered crystal structure. The width of the nanowires is on the scale of 50 nm, and the thickness is in the range of 50 nm–150 nm. This length scales are above 10 nm, where hybridization of the topological surface states followed by a gap opening at the Dirac point appears.[19,20] The length can be as long as several tens of micrometers. The nanowire presented in Fig. 2(a) has a total length of 36 μm. The Bi_2Se_3 nanowires are grown in the [110] direction as a single-crystal structure and have a smooth surface. The chemical composition can be characterized using an energy dispersive spectrometer in the scanning TEM mode. The measured ratio is 2:3 as expected for Bi_2Se_3. The grown nanowires are mechanically transferred onto a Si (111) substrate, and the gold contacts separated by a 14 μm gap are fabricated on top of the nanowire by lithography. Figure 2(a) shows a micrograph of one of the nanowire devices with two contacts, which are connected to two gold pads on the left- and right-hand sides of the nanowire.[21] The sample is mounted with silver paste onto a chip carrier and connected with 25 nm diameter gold wires by wire bonding.

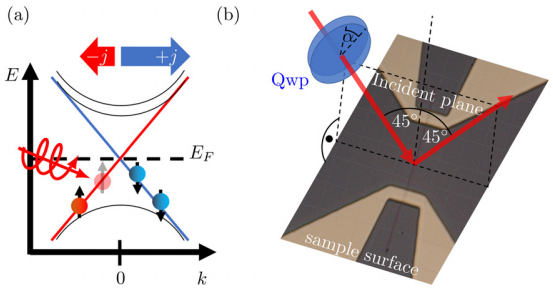

FIG. 1. (a) depicts a schematic band structure of Bi_2Se_3 in the presence of the circular photogalvanic effect. The asymmetric population of the surface states (implied by the unequal number of red and blue dots) is generated by the absorbed circular polarized light (red arrow) and generates a net spin-polarized electrical current due to spin momentum locking. In (b), the setup geometry is depicted. The red arrows represent the incoming and reflected beam that hits the sample surface at an angle of incident of 45°. The polarization of the exciting light changes with the angle α of the qwp.

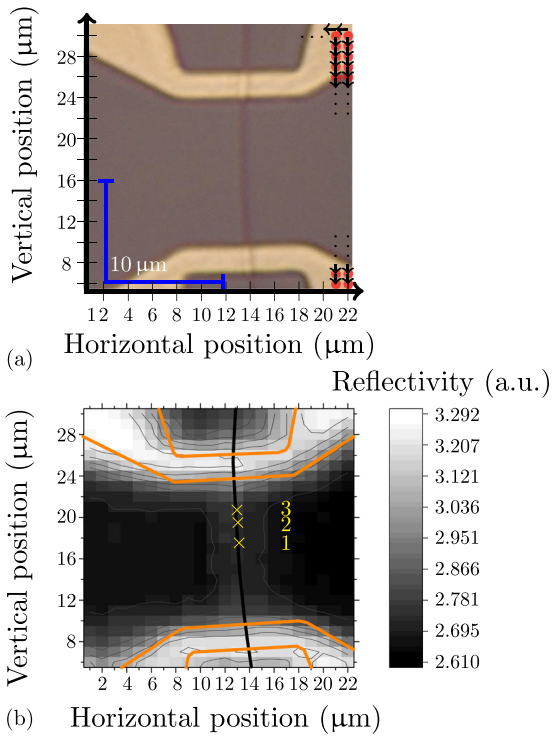

FIG. 2. (a) shows a light microscopy image of the used sample. The nanowire (dark gray vertical line) is placed on a Si (111) substrate (gray). The gold contacts (yellow) are on top of the nanowire. The two closer parallel edges of the gold contacts are separated by 14 μm. The red dots mark the center of the laser spot on the sample surface. The actual FWHM of the laser spot is four times larger than the dots. The black arrows indicate the direction of the movement of the laser spot. The raster pattern starts at (22, 30) and ends at (1, 6). (b) The edges of the gold contacts (orange) and the position of the nanowire (black line) are marked on the spatially resolved reflected light intensity. Three positions on the nanowire are marked and numbered by 1, 2, and 3 (yellow).

The light source for the photocurrent measurements is a diode laser with a wavelength of 785 nm (1.55 eV) modulated at a frequency of 77 Hz. The laser light passes through a linear polarizer and a quarter-wave plate (qwp) prior to impinging on the sample surface at an angle of incidence of 45°. The rotation angle α of the qwp is controlled by a step motor to change the polarization of the excitation beam [see Fig. 1(b)]. The laser light is focused down to $(4.3\pm0.11)\,\mu m \times (2.89\pm0.08)\,\mu m$ on the sample surface. The intensity of the light reflected from the sample surface is measured using a photodiode. The photocurrent between the two contacts and the light reflected from the sample surface are simultaneously measured using a lock-in amplifier. The laser spot can be moved across the sample surface along the vertical and horizontal directions by two step motors with a minimum step size smaller than 1 μm and an error of 200 nm. The raster pattern of the laser spot (red dots) is depicted in Fig. 2(a), as drawn in a light microscopy image of the sample. The measurement starts with the laser spot in the right upper corner [position (22, 30) in Fig. 2(a)]. Then, the qwp is rotated by $\Delta\alpha = 6^\circ$ steps to carry out a full

rotation, while the photovoltage and the intensity of the reflected beam are measured. Afterwards, the laser spot is moved down by 1 μm to the position (22, 29) as depicted by the raster pattern in Fig. 2(a), repeating the measurement procedure until the bottom left position is reached.

For each data point in the two-dimensional voltage maps, the photovoltage between the two contacts is measured, while the qwp is rotated by 360° in total, changing the polarization from linear polarized ($\alpha = 0°$), to left-circular polarized ($\alpha = 45°$), to linear polarized ($\alpha = 90°$), to right-circular polarized ($\alpha = 135°$), to linear polarized ($\alpha = 180°$), to left-circular polarized ($\alpha = 225°$), and so on and so forth (the characterization of the qwp is given in the supplementary material in Fig. S1). The measured photovoltage v is a sum of four contributions,

$$v(\alpha) = C\sin(2\alpha) + L_1\sin(4\alpha) + L_2\cos(4\alpha) + D. \quad (1)$$

The contributions in Eq. (1) can be distinguished by their dependence on the polarization of the exciting laser light, as it has been done previously by McIver *et al.* for photocurrent measurements in the exfoliated Bi_2Se_3 Hall bar devices.[11] The first term $C\sin(2\alpha)$ of Eq. (1) modulates the difference in the photovoltage for left and right circular polarized light and is zero if the exciting light is linear polarized. According to McIver *et al.*, this term describes the amount of spin-polarized voltage generated by the CPGE, while previous measurements by Shalygin *et al.*[22] show that the circular photon drag effect can also cause a similar voltage in (110)-grown quantum wells. In this paper, we relate the first term in Eq. (1) to the CPGE following the notation of recent works.[11,23] Therefore, the magnitude of amplitude C, which is half of the difference between the photovoltage for different helicities (see Fig. 3), is used as a measure for the size of the spin-polarized voltage. The second term $L_1\sin(4\alpha)$ and third term $L_2\cos(4\alpha)$ describe the contributions that arise from the linear photogalvanic effect and the photon drag effect.[11,24,25] As we show below, the last term D is independent of the polarization and arises from the Seebeck effect. Possible contributions of polarization independent photogalvanic and photon drag effects are negligible. The polarization dependent absorption is modulated by the third term (see Fig. S2 in the supplementary material). The Seebeck effect is caused by heating due to the laser spot, which is smaller than the distance between the gold contacts and, therefore, creates an overall temperature gradient that can change the direction and size as the laser spot is moved across the sample surface. In the following, Eq. (1) is the fitfunction and the four amplitudes C, L_1, L_2, and D are determined by fitting Eq. (1) to the measured photovoltage at every laser spot position. The resulting fitfunctions and the measured photovoltage for three positions are shown in Fig. 3, and the results for all four parameters are shown in Fig. S3 in the supplementary material. The horizontal and vertical positions of the laser spot are then used as the spatial coordinates for the extracted amplitudes as in Fig. 4 for the thermoelectric contribution represented by D and the spin-polarized contribution represented by C. At the same time, the intensity of the reflected light for every value of the photovoltage is measured using a second lock-in amplifier. Instead of fitting Eq. (1) to the obtained values, we take the value for a fixed polarization at $\alpha = 0°$ and again use the position of the laser spot as the coordinates for the reflectivity to obtain a two-dimensional map of the reflectivity [see Fig. 2(b)], which allows us to identify the positions of the nanowires and the gold contacts.

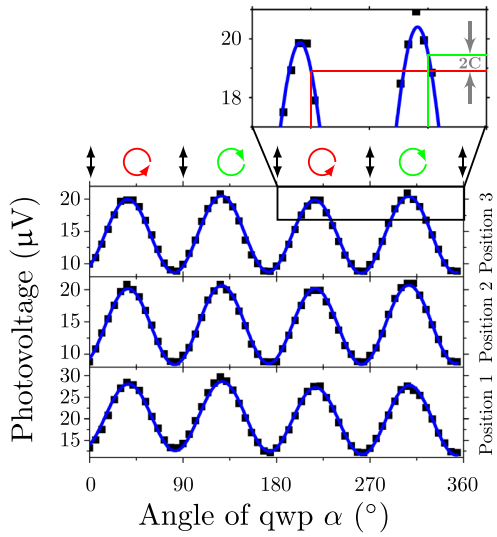

FIG. 3. The measured photovoltage (black squares) and the analysis results using Eq. (1) (blue line) as a function of the rotation angle α for three laser spot positions [see Fig. 2(b)] are displayed. In addition, the photovoltages for left and right circular polarized light (indicated by green and red lines) are marked. The difference between these photovoltage values is equal to 2C. The results for the parameter in Eq. (1) are shown in Fig. S3 in the supplementary material.

In the reflectivity map [Fig. 2(b)], three different areas can be distinguished. The area with the highest intensity (white) shows the position of the Au contacts, while the region with the lowest reflectivity (black) represents the 300 nm SiO on top of the Si substrate. The nanowire can be clearly distinguished between the contacts (in dark gray). Its size looks exaggerated since its width (150 nm) is smaller than the spot size of the laser beam, and so it acts as a scattering center. Therefore, the reflectivity map proves that the area shown in Fig. 2(a) is illuminated and indicates the position of the nanowire. The nanowire is marked in the photovoltage maps (Fig. 4) by a black line.

The three selected photovoltage measurements in Fig. 3 at three different positions along the nanowire [marked in yellow in Fig. 2(b)] show good agreement between Eq. (1) and the measured voltage. It is also observed that thermoelectric contribution D, which is equal to the shift along the vertical direction, is at least one order of magnitude larger than spin-polarized contribution C. The spatially resolved maps in Fig. 4 enable a more detailed inspection of the two contributions. The thermoelectric amplitude D [Fig. 4(a)] changes its sign from positive at the top electrode to negative at the lower electrode. Note that the thermoelectric current that creates the thermoelectric voltage is generated by two temperature gradients with opposite signs that point from the laser spot position toward the two colder contacts. Therefore, the position of the laser spot with respect to the contacts determines the size and sign of the thermoelectric voltage. When the laser spot is in the center between the contacts, the two temperature gradients cancel, and thus, the net temperature gradient and D vanish. In our measurements [Fig. 4(a)], the direction of the net temperature gradient is encoded in red and blue, corresponding to the gradients pointing toward the lower or upper contacts, respectively. At the vertical position of 13 μm in Fig. 4(a), the thermoelectric contribution D becomes

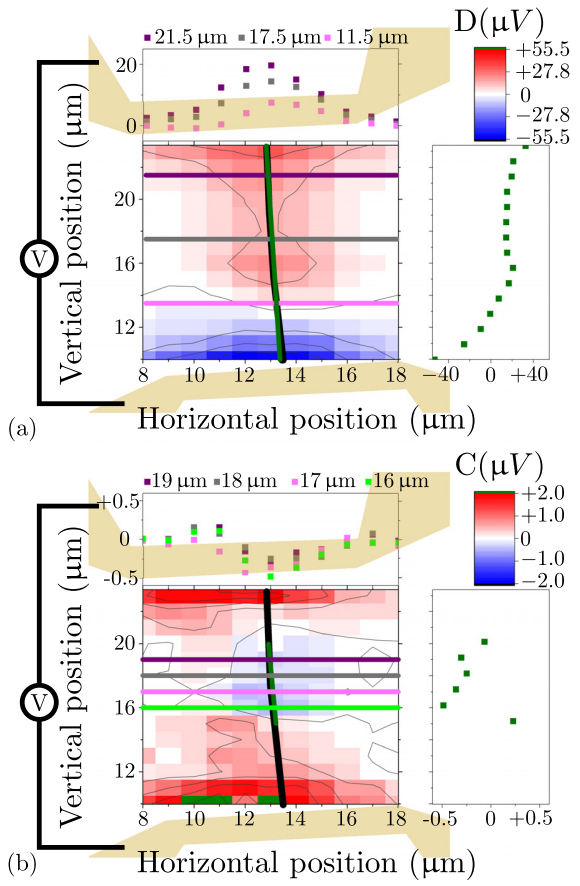

FIG. 4. (a) The map shows the amplitude D related to the thermoelectric voltage at different laser spot positions in the 14 μm gap between the gold contacts. The vertical contour plot shows the amplitude D along the nanowire position, and the horizontal contour plots show how the thermoelectric voltage drops when the center of the laser spot is moved away from the nanowire. (b) The map shows the spatially resolved amplitude C, related to the spin-polarized current. The vertical contour plot shows the spin-polarized voltage along the nanowire (green line), and the four horizontal contour plots prove that the spin-polarized voltage increases when the nanowire is illuminated.

zero. Once the laser spot is moved toward one of the electrodes, the net temperature gradient is nonzero, and a net current is generated by the Seebeck effect. The sign of the thermoelectric current changes from top to bottom since the direction of the net temperature gradient is reversed. Thus, the voltage of the contour plot in the vertical direction along the nanowire changes its sign from top to bottom [shown in Fig. 4(a)]. The contour plots perpendicular to the nanowire reveal that the highest values of D are reached when the center of the laser spot matches the horizontal position of the nanowire at 13 μm. If the laser spot center is moved away from the nanowire along the horizontal direction, then the values decrease. When the laser spot center is 4 μm, which is equal to the full width at half maximum (FWHM) of the laser spot diameter, or further away from the nanowire, the thermovoltage drops down to nearly zero. This means that there is no contribution to thermoelectric contribution D transferred through the substrate.

A slight enhancement of the voltage is observed when not only the nanowire but also the nanowire underneath the gold contact is partially illuminated. This appears for the vertical positions above 21 μm and below 11 μm and is manifested by the nonlinear increase in the photovoltage in the vertical contour plot and also by the circular shape of the lines in the 2D map in Fig. 4(a). In addition, the thermoelectric voltage reaches zero at a vertical position of 13 μm, which is 4 μm away from the geometric center of the nanowire. One possible reason for this shift of zero-crossing might be the asymmetrical heating of the laser beam since its gaussian heat profile is no longer symmetrical due to the angle of incidence of 45°. Another reason might be the enhancement of the thermoelectric voltage at the Au/TI layer combined with the laser spot size. The FWHM of the laser spot in the vertical direction is 2.89 μm. When the center of the laser is 3 μm away from the contacts, the Au/TI layer is still heated and contributes to the measured thermoelectric voltage. As a result, the slope toward the lower contact (negative photovoltage) is steeper compared to the slope toward the higher contact (positive photovoltage). In addition, the nanowire in this experiment slightly bends as shown in Fig. 4(a) and the thermoelectric voltage changes drastically, when the laser spot is moved in the horizontal direction. Hence, the center of the laser light might not always match to the center of the nanowire when moved in the vertical direction, leading to small changes in the thermoelectric voltage. This enhancement of photovoltage when illuminating a nanowire underneath a metallic contact is also observed for measurements of GaN, ZnO, and Si nanowires. In these materials, the observed increase is a result of the Schottky effect.[26–28] In our case, the gold contact is metallic and the TI can act as a semiconducting layer. The sign of the current caused by band bending at the metal/semiconductor interface changes between the contacts since the band bending is symmetrical with regard to the center of the nanowire; this is in good agreement with the behavior of thermoelectric voltage D observed in this work.

To exclude the influence of the contacts, we focus on the spin-polarized contribution C in this work in the area between 15 and 20 μm along the vertical axes displayed in Fig. 4(b) in green. The contour plots along the horizontal direction show that the spin-polarized voltage C decreases when the center of the laser spot does not match the position of the nanowire at the horizontal position of 13 μm. This proves that the substrate does not contribute to the spin-polarized voltage. The largest value with a modulus of 0.5 μV is reached when the laser spot center matches the nanowire, which is a factor of 80 smaller than the largest value for the thermoelectric contribution $D = 40$ μV. The largest values are reached on the small plateau shown in the vertical contour plot over a range of 4 μm. Closer to the contacts, the spin-polarized voltage decreases.

In summary, we performed photocurrent measurements on Bi_2Se_3 nanowires and analyzed the spatially resolved results for the spin-polarized and thermoelectric contributions. For the thermoelectric contribution, we observe a sign change of D along and on the nanowire. This indicates that the parameter D is dominated by the Seebeck effect and potential contributions of polarization independent photogalvanic and photon drag effects are negligible. In addition, we detect an enhancement of the thermoelectric and the spin-polarized contribution when the nanowire underneath the gold contacts is illuminated in comparison to illuminating only the TI. We also show that spin-polarized currents can be generated in nanowires within the range of 5 μm along the nanowire by using circular polarized light.

Thus, we have demonstrated the ability to drive photogalvanic currents in nanowires, which shows their promising potential for use in photospintronic applications in the future.

See the supplementary material for the characterization of the qwp, more information about the polarization dependent absorption, and the results for the parameters C, L_1, L_2, and D for position 1, 2, and 3 in Fig. 2(b).

We are grateful to the German Science Foundation (DFG) for financial support through priority program SPP1666: "Topological insulators: materials, fundamental properties, devices" (No. MU1780/10-2).

REFERENCES

[1]C. L. Kane and E. J. Mele, "Z_2 topological order and the quantum spin hall effect," Phys. Rev. Lett. **95**, 146802 (2005).
[2]M. König, S. Wiedmann, C. Brüne, A. Roth, H. Buhmann, L. W. Molenkamp, X.-L. Qi, and S.-C. Zhang, "Quantum spin Hall insulator state in HgTe quantum wells," Science **318**, 766–770 (2007).
[3]M. Z. Hasan and C. L. Kane, "Colloquium: Topological insulators," Rev. Mod. Phys. **82**, 3045–3067 (2010).
[4]Y. Huang, Y. Song, S. Wang, I. Buyanova, and W. Chen, "Spin injection and helicity control of surface spin photocurrent in a three dimensional topological insulator," Nat. Commun. **8**, 15401 (2017).
[5]L. Plucinski, G. Mussler, J. Krumrain, A. Herdt, S. Suga, D. Grützmacher, and C. M. Schneider, "Robust surface electronic properties of topological insulators: Bi_2Te_3 films grown by molecular beam epitaxy," Appl. Phys. Lett. **98**, 222503 (2011).
[6]D. Biswas, S. Thakur, G. Balakrishnan, and K. Maiti, "Exceptional surface and bulk electronic structures in a topological insulator, Bi_2Se_3," Sci. Rep. **5**, 17351 (2015).
[7]J. Krumrain, G. Mussler, S. Borisova, T. Stoica, L. Plucinski, C. Schneider, and D. Grützmacher, "MBE growth optimization of topological insulator Bi_2Te_3 films," J. Cryst. Growth **324**, 115–118 (2011).
[8]Z.-H. Pan, E. Vescovo, A. V. Fedorov, D. Gardner, Y. S. Lee, S. Chu, G. D. Gu, and T. Valla, "Electronic structure of the topological insulator Bi_2Se_3 using angle-resolved photoemission spectroscopy: Evidence for a nearly full surface spin polarization," Phys. Rev. Lett. **106**, 257004 (2011).
[9]J. Sobota, S.-L. Yang, D. Leuenberger, A. Kemper, J. Analytis, I. Fisher, P. Kirchmann, T. Devereaux, and Z.-X. Shen, "Ultrafast electron dynamics in the topological insulator Bi_2Se_3 studied by time-resolved photoemission spectroscopy," J. Electron Spectrosc. Relat. Phenom. **195**, 249–257 (2014).
[10]M. Romanowich, M.-S. Lee, D.-Y. Chung, S. D. Mahanti, M. G. Kanatzidis, and S. H. Tessmer, "Interplay of topological surface and bulk electronic states in Bi_2Se_3," Phys. Rev. B **87**, 085310 (2013).
[11]J. W. McIver, D. C. Hsieh, H. Steinberg, P. Jarillo-Herrero, and N. Gedik, "Control over topological insulator photocurrents with light polarization," Nat. Nanotechnol. **7**, 96–100 (2012).
[12]S. D. Ganichev and W. Prettl, "Spin photocurrents in quantum wells," J. Phys. **15**, R935–R983 (2003).
[13]C. Kastl, C. Karnetzky, H. Karl, and A. W. Holleitner, "Ultrafast helicity control of surface currents in topological insulators with near-unity fidelity," Nat. Commun. **6**, 6617 (2015).
[14]K. N. Okada, N. Ogawa, R. Yoshimi, A. Tsukazaki, K. S. Takahashi, M. Kawasaki, and Y. Tokura, "Enhanced photogalvanic current in topological insulators via fermi energy tuning," Phys. Rev. B **93**, 081403 (2016).
[15]H. Plank, S. N. Danilov, V. V. Bel'kov, V. A. Shalygin, J. Kampmeier, M. Lanius, G. Mussler, D. Grützmacher, and S. D. Ganichev, "Opto-electronic characterization of three dimensional topological insulators," J. Appl. Phys. **120**, 165301 (2016).
[16]L. Braun, G. Mussler, A. Hruban, M. Konczykowski, T. Schumann, M. Wolf, M. Münzenberg, L. Perfetti, and T. Kampfrath, "Ultrafast photocurrents at the surface of the three-dimensional topological insulator Bi_2Se_3," Nat. Commun. **7**, 2041–1723 (2016).
[17]P. Seifert, K. Vaklinova, K. Kern, M. Burghard, and A. Holleitner, "Surface state-dominated photoconduction and THz generation in topological Bi_2Te_2Se nanowires," Nano Lett. **17**, 973–979 (2017).
[18]T. Schumann, N. Meyer, G. Mussler, J. Kampmeier, D. Grützmacher, E. Schmoranzerova, L. Braun, T. Kampfrath, J. Walowski, and M. Münzenberg, "Observation of spin Nernst photocurrents in topological insulators," arXiv:1810.12799 (2018).
[19]H. S. Shin, B. Hamdou, H. Reith, H. Osterhage, J. Gooth, C. Damm, B. Rellinghaus, E. Pippel, and K. Nielsch, "The surface-to-volume ratio: A key parameter in the thermoelectric transport of topological insulator Bi_2Se_3 nanowires," Nanoscale **8**, 13552–13557 (2016).
[20]J. Gooth, J. G. Gluschke, R. Zierold, M. Leijnse, H. Linke, and K. Nielsch, "Thermoelectric performance of classical topological insulator nanowires," Semicond. Sci. Technol. **30**, 015015 (2015).
[21]B. Hamdou, J. Gooth, A. Dorn, E. Pippel, and K. Nielsch, "Surface state dominated transport in topological insulator Bi_2Te_3 nanowires," Appl. Phys. Lett. **103**, 193107 (2013).
[22]V. A. Shalygin, H. Diehl, C. Hoffmann, S. N. Danilov, T. Herrle, S. A. Tarasenko, D. Schuh, C. Gerl, W. Wegscheider, W. Prettl, and S. D. Ganichev, "Spin photocurrents and the circular photon drag effect in (110)-grown quantum well structures," JETP Lett. **84**, 570–576 (2007).
[23]S. Luo, L. He, and M. Li, "Spin-momentum locked interaction between guided photons and surface electrons in topological insulators," Nat. Commun. **8**, 2141 (2017).
[24]P. Olbrich, L. E. Golub, T. Herrmann, S. N. Danilov, H. Plank, V. V. Bel'kov, G. Mussler, C. Weyrich, C. M. Schneider, J. Kampmeier, D. Grützmacher, L. Plucinski, M. Eschbach, and S. D. Ganichev, "Room-temperature high-frequency transport of Dirac fermions in epitaxially grown Sb_2Te_3- and Bi_2Te_3- based topological insulators," Phys. Rev. Lett. **113**, 096601 (2014).
[25]H. Plank, L. E. Golub, S. Bauer, V. V. Bel'kov, T. Herrmann, P. Olbrich, M. Eschbach, L. Plucinski, C. M. Schneider, J. Kampmeier, M. Lanius, G. Mussler, D. Grützmacher, and S. D. Ganichev, "Photon drag effect in $(Bi_{1-x}Sb_x)_2Te_3$ three-dimensional topological insulators," Phys. Rev. B **93**, 125434 (2016).
[26]F. Léonard, E. Song, Q. Li, B. Swartzentruber, J. A. Martinez, and G. T. Wang, "Simultaneous thermoelectric and optoelectronic characterization of individual nanowires," Nano Lett. **15**, 8129–8135 (2015).
[27]C. Park, J. Lee, H.-M. So, and W. S. Chang, "An ultrafast response grating structural ZnO photodetector with back-to-back Schottky barriers produced by hydrothermal growth," J. Mater. Chem. C **3**, 2737–2743 (2015).
[28]Y. Ahn, J. Dunning, and J. Park, "Scanning photocurrent imaging and electronic band studies in silicon nanowire field effect transistors," Nano Lett. **5**, 1367–1370 (2005).

Supplementary Material: Photocurrent measurements in topological insulator Bi_2Se_3 nanowires

N. Meyer,[1] K. Geishendorf,[2] J. Walowski,[1] A. Thomas,[2] and M. Münzenberg[1]

[1)] *Institute of Physics, University Greifswald, Felix-Hausdorff-Str. 6, 17489 Greifswald, Germany*

[2)] *IFW Dresden, Institute for Metallic Materials, Helmholtzstrae 20, 01069 Dresden, Germany*

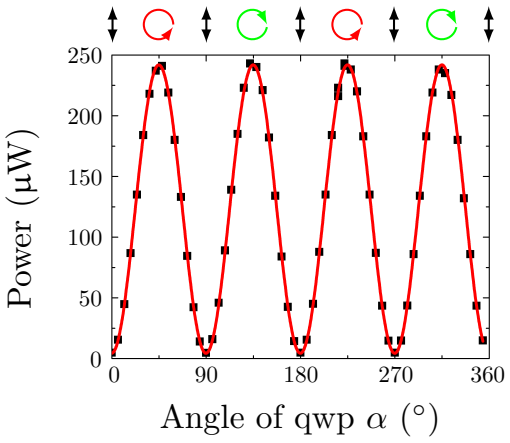

FIG. S1. The characterization of the used qwp is presented. The measurement setup consists of one linear polarizer, the qwp, a second linear polarizer (analyzer) rotated by 90° with respect to the first linear polarizer, and an optical power meter. During the measurements the two linear polarizers and the power meter are fixed, while the qwp is rotated stepwise by 360°. The measured power is than displayed together with the angle α of the qwp. The measured power is minimal when the light leaving the qwp is linear polarized perpendicular to the orientation of the analyzer and reaches it maximum, when the light leaving the qwp is circular polarized. The resulting polarization behind the qwp is sketched by the arrows (black, green and red) on top of the graph. The analyzer and the power meter are removed from the setup when the photo current measurements are carried out. The linear polarizer in front of the qwp and the qwp remain within the setup.

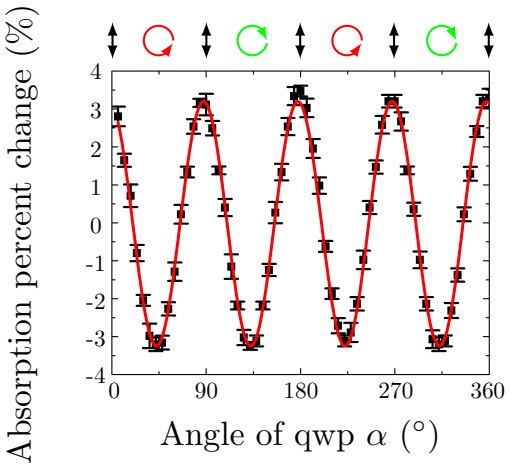

FIG. S2. The percent change of the absorption (black squares) calculated by the measured reflected intensity is displayed averaged over eight different positions along and on the nanowire between the contacts. The absorption percent change for the linear polarized light for $\alpha = 90°, 180°, 270°$ and $360°$ and for the circular polarized light $\alpha = 45°, 135°, 225°,$ and $315°$ is constant with respect to the statistic errors. The modulation of the absorption matches a $\cos(4\alpha)$ function (red line) which is in good agreement with the term $L_2 \cos(4\alpha)$ in Eq.(1) in the main manuscript. Hence, the polarization dependence of the Seebeck effect is modulated by the term $L_2 \cos(4\alpha)$.

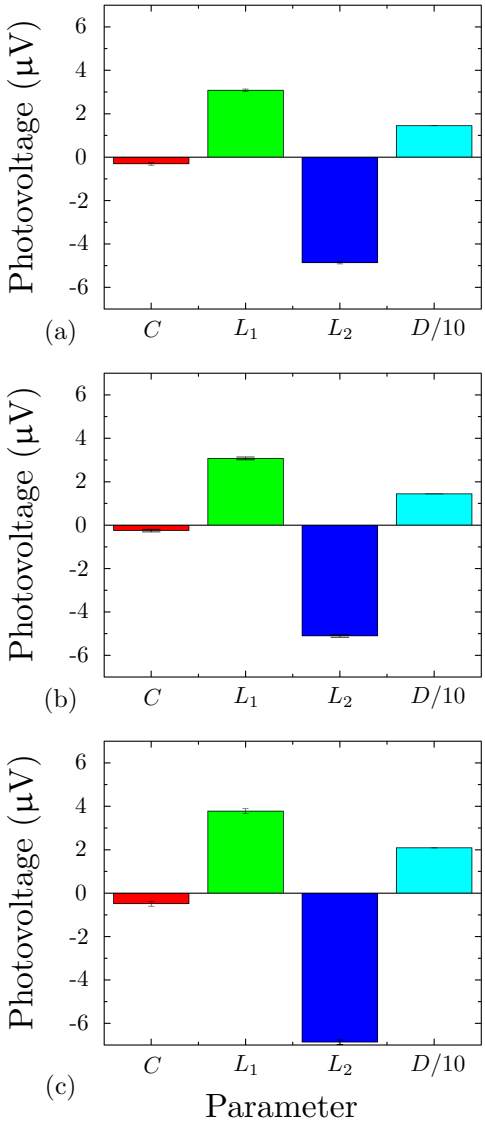

FIG. S3. The results for the parameters C, L_1, L_2 and D for (a) position 3, (b) position 2 and (c) position 1 in FIG. 2(b) in the main manuscript are displayed. The values for D are divided by a factor of 10.

3.3 The impact of metallic contacts on spin-polarized photocurrents in topological insulator Bi_2Se_3 nanowires

Applied Physics Letters ARTICLE scitation.org/journal/apl

The impact of metallic contacts on spin-polarized photocurrents in topological insulator Bi_2Se_3 nanowires

Cite as: Appl. Phys. Lett. **117**, 262401 (2020); doi: 10.1063/5.0019044
Submitted: 23 June 2020 · Accepted: 8 December 2020 ·
Published Online: 28 December 2020

N. Meyer,[1,a)] K. Geishendorf,[2] J. Walowski,[1] A. Thomas,[2,3] and M. Münzenberg[1]

AFFILIATIONS

[1]Institute of Physics, University of Greifswald, Felix-Hausdorff-Str. 6, 17489 Greifswald, Germany
[2]IFW Dresden, Institute for Metallic Materials, Helmholtzstraße 20, 01069 Dresden, Germany
[3]Institute of solid state and materials physics, Technische Universität Dresden, 01062 Dresden, Germany

[a)]Author to whom correspondence should be addressed: nina.meyer@uni-greifswald.de

ABSTRACT

Recently, a quantum phase, the topological insulator, has been vividly investigated in a variety of materials. Its unique band structure allows for optical generation and control of spin-polarized currents based on the circular photogalvanic effect. In this paper, we generate and distinguish the different photocurrent contributions via the polarization of the driving light wave. We discuss the helicity-dependent spin-polarized current and the polarization-independent thermoelectric current as spatially resolved maps, focusing on the influence of the topological insulator/metallic contact interface. We observe for both current contributions a significant enhancement of the current values at the topological insulator/metallic contact interface. In the case of the thermoelectric current, the enhancement is localized at the center of the interface. The spin-polarized current reaches two extrema per contact, which differ by their sign and are localized nearby the contact edges. We discuss the general behavior of the thermovoltage as a three-material Seebeck effect and explain the enhanced values by the acceleration of the photoelectrons generated in the space charge region of the topological insulator/metallic contact interface. Furthermore, we interpret the temperature gradient together with the spin Nernst effect as a possible origin for the enhancement and spatial distribution of the spin-polarized current.

Recently, topological order gained a lot of attention among physicists after the discovery of topological insulators (TIs)[1–3] in solid state materials. This additional state of quantum matter differs from trivial insulators by hosting a bulk energy gap, while the surface possesses gapless electronic states. The nanowires investigated in this paper consist of Bi_2Se_3. This material is a three-dimensional topological insulator with time-reversal symmetry.[4,5] Thus, the surface states of Bi_2Se_3 are helical and the spin degeneracy is lifted at the surface. Also the backscattering of the surface electrons is suppressed.[6,7] Those three properties make Bi_2Se_3 a promising candidate for spintronics- or optoelectronics applications.

The surface states make those materials suitable for polarization-sensitive detectors based on the polarization-dependent photovoltaic or photogalvanic effects.[8,9] Both effects are based on creating an asymmetric population of the spin-polarized surface states. Since the momentum and spin orientation are locked at the surface, the asymmetry in the surface state population generates a spin-polarized electrical current. When the asymmetry is generated by exciting the surface states with circular-polarized light, the effect is known as the circular photogalvanic effect (CPGE).[10] The CPGE has been observed in several optoelectronic experiments, which demonstrate the direction control of spin-polarized currents by circular-polarized light in TI materials.[11–13] The dimensions of those investigated TIs are in the micrometer range. Little is known about those effects when the dimensions of TIs decrease toward the nanometer scale, e.g., in nanowires. There is one example for all-optical control in Bi_2Te_3Se nanowires by Seifert *et al.*[13] They observe an enhancement of the THz amplitude in the vicinity of the gold contacts which they explain by a locally enhanced spin-polarized current. In a previous work, we measured the polarization-dependent photocurrent while scanning the Bi_2Se_3 nanowire.[14] We observed that the polarization-independent current contribution is dominated by the Seebeck effect. We also detect a helicity-dependent current contribution caused by the CPGE. In both cases, we observed that the values of the contributions increase in the vicinity of the gold contacts, but we did not discuss the origin in detail. In this paper, we explicitly discuss the influence of the metallic

contacts on the thermoelectric and spin-polarized current. We generate the two-dimensional scans for both contributions to discuss the origin of their enhancement close to the topological insulator/metallic contact interface.

The photoelectric measurements in this paper are performed on Bi_2Se_3 nanowires synthesized by the gold-catalyzed vapor–liquid–solid method (for more details on the nanowire growth, see Shin *et al.*[15]). The nanowires are grown in the [110] direction as single-crystal structures assuring a smooth surface. The nanowire width is on the order of 50 nm and the thickness spans from 50 nm to 150 nm, thus hybridization of the topological surfaces states can be excluded.[15,16] The nanowires are transferred mechanically to a Si(111) substrate with 100 µm of SiO_x. The contact pads of 5 nm Cr underneath 50 nm Au are patterned on top of the nanowire with a spacing of 14 µm. The photoelectric measurements are recorded using a well-established lock-in technique. The light source is a diode laser with a wavelength of 785 nm (1.55 eV) modulated at 77 Hz by a square-function generator. The laser beam is guided through a linear polarizer combined with a rotatable quarter-wave plate (qwp) for polarization control before impinging at an angle of incidence of $\theta = 45°$ on the sample surface. The laser light is focused down to a spot size of (2.9 ± 0.08) µm $\times (3.4 \pm 0.12)$ µm on the sample surface. The measured photocurrent $j(\alpha)$ [photovoltage $v(\alpha)$] is mapped to the polarization state via the qwp rotational angle α. Thus, the photocurrent is measured at fixed positions (k,j) for linear, left-circular, and right-circular polarized light, scanning the sample surface vertically and horizontally by moving the laser across the sample surface with stepper motors. At the same time, the light intensity reflected from the sample surface $I(\alpha)$ is recorded by a second lock-in amplifier via a photodiode. The qwp rotates at every laser spot position (k,j) from $\alpha = 0, \Delta\alpha, \ldots, 360°$ with a step size of $\Delta\alpha = 6°$. Afterwards, the laser spot is moved in the vertical direction by $\Delta j = 1$ µm to the next position $(k, j - \Delta j)$. There, the photocurrent $j(\alpha)$ and the reflected intensity $I(\alpha)$ are measured again for a full qwp rotation. This generates a set of 60 current (voltage) values at each position (j,k) as presented in Fig. 1(a).

The data are evaluated by identifying the contributions in the measured photocurrent (voltage) by their polarization dependence. We use the ansatz suggested by McIver *et al.*[11] that includes four contributions:

$$j(\alpha) = C \sin(2\alpha) + L_1 \sin(4\alpha) + L_2 \cos(4\alpha) + D. \quad (1)$$

In our measurements, the laser light is linear polarized at $\alpha = 0, 90, 180, 270$ and 360°, left-circular polarized σ^+ at $\alpha = 45$ and 225°, and right-circular polarized σ^- at $\alpha = 135$ and 345°. The term $C \sin(2\alpha)$ in Eq. (1) represents the spin-polarized helicity-dependent current. The amplitude $2C$ is the photocurrent difference between σ^+- and σ^--light. The qwp phase is set so that $\sin(2\alpha)$ is zero for linear polarized light. The physical origin of this term is still under discussion. Measurements by Shalygin *et al.* on (110)-grown GaAs/AlGaAs quantum wells prove that the circular photon drag effect can cause a helicity-dependent current,[17] while later measurements on exfoliated Bi_2Se_3 Hall bar devices by McIver *et al.*[11] relate the helicity-dependent currents to the CPGE. The lifted spin degeneracy of surface electrons in a TI enables to generate an asymmetrical population of the spin-polarized surface states in the k-space by circular polarized light, since the optical selection rules for interband transitions have to be fulfilled. The asymmetric populated surface states cause an

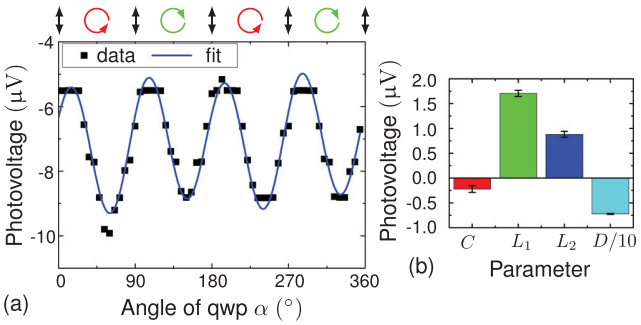

FIG. 1. Measured photovoltage $v(\alpha)$ for $\alpha = 0, \Delta\alpha, \ldots, 360$ with $\Delta\alpha = 6°$ at position (17,8) in Fig. 3(d). In (a), the measured data (black squares) and the fit function (blue line) are displayed. The arrows represent the polarization state of the laser light. In (b), the fitting parameters C, L_1, L_2 and $D/10$ and their uncertainties are displayed.

electrical spin-polarized current, since the spin and its momentum are locked on the surface of a TI. That exciting the spin-polarized surface states optically can lead to spin-polarized photocurrents has among others been demonstrated by Takeno *et al.*[18] by performing time-domain terahertz wave measurements and time-resolved magneto-optical Kerr rotation measurements. Hence, it is possible to generate a measurable helicity-dependent photocurrent due to the CPGE, which is spin-polarized.[10,12,13,19–21] Therefore, we relate the first term $C \sin(2\alpha)$ in Eq. (1) to the CPGE following the notation established in the recent studies[11,22] and discuss the amount of spin-polarized current by displaying the amplitude C.

The second term $L_1 \sin(4\alpha)$ and third term $L_2 \cos(4\alpha)$ in Eq. (1), have a different frequency than the first term. Thus, they do not affect the first term. The third term $L_2 \cos(4\alpha)$ represents the polarization-dependent absorption. The physical effects related to the two contributions are still under discussion both being sometimes related to the linear photogalvanic effect or the photon drag effect.[11,23,24] The last term D is polarization-independent and can originate from the polarization-independent photogalvanic effect, the photon drag effect and, due to the laser light heating, the Seebeck effect. We observed in a previous work Ref. 14, that the contributions of the polarization-independent photogalvanic and photon drag effect to the overall behavior of D seem to be small compared to the contribution of the Seebeck effect.

For data analysis, the function $j(\alpha)$ ($v(\alpha)$) is fitted to the experimental data to extract the parameters C, L_1, L_2, and D at each position (j, k) as in Fig. 1(a). The values for the four parameters and their uncertainties are displayed in Fig. 1(b). The parameters C and D are displayed in two dimensional maps as a function of the laser spot position, see Figs. 2(b) and 2(c). The contact pad positions (edges are marked by orange lines) and the nanowire (black line) are determined from the reflectivity data and are in good agreement with the microscope images of the area of interest [see Figs. 2(a), 3(c), and 3(f)]. In the following, we concentrate on the parameters C and D to investigate the influence of the thermoelectric current on the spin-polarized photocurrent and their enhancement in the vicinity of the contact pads.

The two-dimensional map of the parameter D in Fig. 2(b) shows that the thermocurrent reaches the largest values at the crossing of the nanowire and the contacts. This is visible in the contour plots in gray

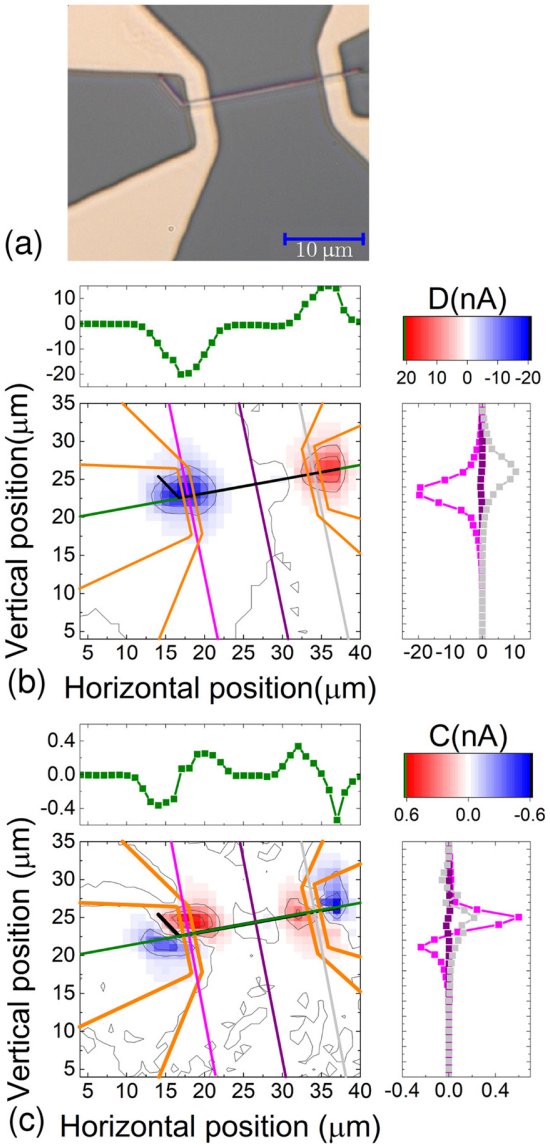

FIG. 2. Photocurrent measurement on a Bi_2Se_3 nanowire with a 14 μm gap with the drain (source) electrode on the right (left). (a) shows the micrograph of the measured area. The spatially resolved results for (b) the thermoelectric current D and (c) the spin-polarized current C are presented, including contour plots along the nanowire (green lines), the contacts (pink and gray lines) and through the center of the nanowire (violet lines).

and pink in Fig. 2(b). The contour plot [green line in Fig. 2(b)] along the nanowire demonstrates that the increase is located at the metal contacts. Between the contacts, the thermocurrent changes it sign and the slope of the thermocurrent is small, just like in Ref. 14. When the laser partly illuminates the crossing of the nanowire and metal contact, the thermocurrent increases drastically until it reaches its largest value at a horizontal position of 35 μm. The origin of this enhancement is discussed later in the manuscript.

The current map of the spin-polarized current, represented by the parameter C, is displayed in Fig. 2(c). C is constant in the middle of the nanowire where the contact pads can be neglected and thus the transport is entirely determined by the surface states. This matches prior research.[14] When the laser spot illuminates the nanowire close to the contact pads, the spin-polarized current increases and reaches its extremal values nearby the contact edges.

The measurement was repeated on a second nanowire, maintaining the contact distance and laser conditions, but changing the contact geometry. The results for axisymmetric contacts or point-symmetric contacts are shown in Fig. 3. For the thermoelectric contribution, we observe for both contact geometries enhanced values at the crossing of the contacts and the nanowire. The thermovoltage in Fig. 3(a) reaches $D = 15.13$ μV at the drain electrode and goes down to $D = 0.85$ μV at position (12,7) on the nanowire, which qualitatively matches the findings for the thermoelectric current in Fig. 2. In Figs. 3(b) and 3(e), the voltage C generated by the spin-polarized current for the two contact geometries is displayed. The voltage C reaches a minimum of $C = -1.84$ μV at (22,8) close to the source electrode and decreases to $C = -0.52$ μV at (14,8) at the nanowire center. Nearby the crossing of the contact pad and the nanowire, the voltage C reaches its extrema, which is in good agreement with the results observed in Fig. 2(c). Switching between the axisymmetric and the point-symmetric contacts does not affect the shape of the distribution or the sign of the voltage C at different areas [see Figs. 3(b) and 3(e)].

The two-interface Seebeck effect discussed in the supplementary material explains why the thermovoltage depends linear on the laser spot position. Thus, the two-interface Seebeck effect in the supplementary material explains the linear region of the contour plot in Figs. 3(a) and 3(d) but not the enhancement of the thermovoltage at the metal contacts. Hence, an additional effect is needed to explain the thermovoltage enhancement at the nanowire/contact interface. The bandgap of Bi_2Se_3 is 300 meV which is typical for semiconductors. Therefore, we expect a band bending at the interface as sketched in Fig. 3(g). Due to the band bending, a positive (negative) space charge zone forms at the contact (nanowire) at the interface. When the laser illuminates the nanowire underneath the drain electrode, an electron-hole pair is created. The electron will be accelerated to the drain electrode and the hole to the center of the nanowire, driven by the electric field around the interface. The electrons entering the drain electrode will contribute to the net-positive current when the holes annihilate with electrons, originating from the source electrode. The photoelectrons generated close to the source electrode contribute to the net-negative current, since the electric field of the space charge region changes it sign. The enhancement at the drain electrode has a maximum at position (7,7) and decreases when the laser spot is moved away from this position. The decrease is due to the Gaussian laser intensity profile. When the laser spot is moved away from position (7,7), less photons illuminate the interface and the current contributing to the measured voltage decreases. The same effect appears at the source electrode, but with an opposite sign.

Comparing the position of the extremal voltage C in Fig. 3(e) to the device layout shows that the largest and smallest spin-polarized current values are located at the edges of the contacts. This is similar to our earlier observations[25] on photocurrent measurements on $(Bi_{0.57}Sb_{0.43})_2Te_3$ Hall bars. There we report the accumulation of spin-polarized current at the Hall bar edges, with a different sign at

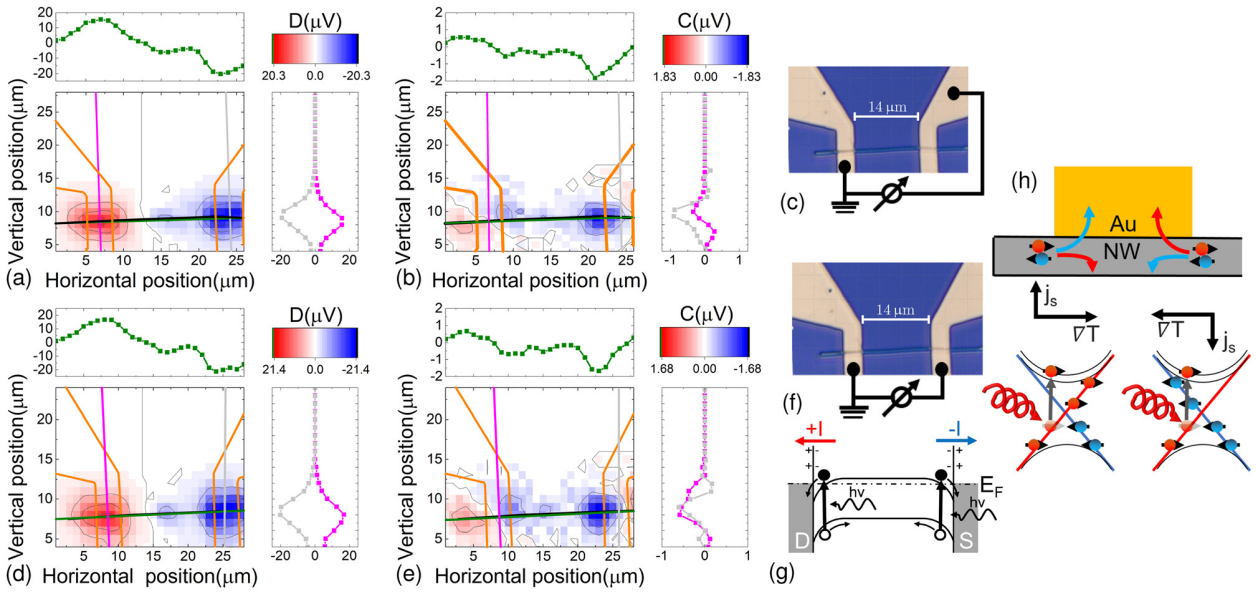

FIG. 3. Photovoltage measurements on a Bi_2Se_3 nanowire for different contacts. In (a), the thermovoltage D and in (b), the voltage C generated by the spin-polarized current for the axisymmetric contacts are displayed. In (c), the axisymetric bonding is marked in black on a micrograph of the sample. In (d), the thermovoltage D and in (e), the voltage C generated by the spin-polarized current are displayed for point-symmetric bonding. The bond position is marked in (f) on a micrograph of the sample. The contour plots along the nanowire (green lines) and along the contacts (pink and gray lines) are displayed next to the maps. In (g), the influence of the band bending at the contact/nanowire interface on the photoelectrons is illustrated. In (h), the two-step process for the spin accumulation at one contact is shown. The deflection of the spin-polarized electrons is sketched in the upper panel and the asymmetric population at the left and right contact edge is shown in the lower panel.

opposite edges. We explained this by the spin Nernst effect, which describes the separation of electrons with opposite spin orientations due to a transverse temperature gradient. How the spin Nernst effect can enhance the values for C in the nanowire (NW) devices is depicted for the drain electrode in Fig. 3(h). When the laser spot illuminates the left edge of the drain electrode the electrons with opposite spin orientations are deflected perpendicular to the temperature gradient ∇T. The spin-up electrons (depicted in blue) are deflected toward the interface and can enter the gold layer. Hence, the population of the Dirac cone is asymmetric, before taking optical transitions into account. At the right edge of the drain electrode, the temperature gradient ∇T points in the opposite direction. Thus, the spin-down electrons (depicted in red) are deflected into the gold layer. This means more surface states are populated by spin-up than spin-down electrons. Taking the optical excitation with left-circular polarized light into account, decreases (increases) the asymmetry of the surface state population at the left (right) edge of the drain electrode. For right-circular polarized light, the asymmetry would increase (decreases) at the left (right) edge of the drain electrode. Since C is the photovoltage difference for left- and right-circular polarized light, it is positive (negative) at the left (right) side of the drain electrode. This leads to an increase in C at the contact edges on top of the nanowire [see Figs. 3(e) and 3(b)]. At the source electrode, the temperature gradient is negative compared to the drain electrode [see Fig. 3(a)]. Hence, we expect a similar distribution of C with opposite sign, i.e., we expect C to be positive (negative) at the right side (left) of the source electrode in Fig. 3(e).

In summary, spatially resolved photocurrent measurements on Bi_2Se_3 nanowires were performed, focusing on the influence of the contact/nanowire interface on the polarization-independent and the spin-polarized current. Photocurrent measurements on several nanowires yield qualitatively similar results. The polarization-independent contribution on the contact/nanowire interface is a combination of the Seebeck effect and the band bending at the contact/nanowire interface. The Seebeck effect explains the sign change of the thermovoltage along the nanowire. The acceleration of the photoelectrons generated in the space charge region of the contact/nanowire interface causes the enhancement. The Gaussian profile of the laser spot leads to the radial symmetry of the enhancement located at the nanowire contact crossing. We observe for the spin-polarized current C (or voltage C generated by a spin-polarized current, respectively) a constant region in the middle of the nanowire and an enhancement of the current at the contact edges together with a sign change of the spin-polarized current at each contact. The enhancement of the spin-polarized current close to the nanowire/metallic contact interface might be caused by the spin Nernst effect. We show that the influence of the gold contacts to the overall behavior of the nanowire is significant. The enhancement of the spin-polarized current, created in the vicinity of the contact pads, is in good agreement with the findings reported by Seifert *et al.*[13] However, in our low excitation regime, the enhancement is caused by band-bending effects at the contact/nanowire interface and the spin Nernst effect. Enhancing spin-polarized currents in TI nanowires opens up further possibilities for spin current engineering, e.g., generating circular-polarized THz radiation by crossed nanowires.

See the supplementary material for the discussion of the two-interface Seebeck model for the nanowire devices.

We are grateful to the German Science Foundation (DFG) for financial support through the priority program SPP1666: 'Topological insulators: materials, fundamental properties, devices' (No. MU1780/10-2).

DATA AVAILABILITY

The data that support the findings of this study are available from the corresponding author upon reasonable request.

REFERENCES

[1]D. J. Thouless, M. Kohmoto, M. P. Nightingale, and M. den Nijs, "Quantized Hall conductance in a two-dimensional periodic potential," Phys. Rev. Lett. **49**, 405–408 (1982).
[2]C. L. Kane and E. J. Mele, "Z_2 topological order and the quantum spin Hall effect," Phys. Rev. Lett. **95**, 146802 (2005).
[3]M. König, S. Wiedmann, C. Brüne, A. Roth, H. Buhmann, L. W. Molenkamp, X.-L. Qi, and S.-C. Zhang, "Quantum spin Hall insulator state in HgTe quantum wells," Science **318**, 766–770 (2007).
[4]H. Zhang, C.-X. Liu, X.-L. Qi, X. Dai, Z. Fang, and S.-C. Zhang, "Topological insulators in Bi_2Se_3, Bi_2Te_3 and Sb_2Te_3 with a single Dirac cone on the surface," Nat. Phys. **5**, 438–442 (2009).
[5]Y. Xia, D. Qian, D. Hsieh, L. Wray, A. Pal, H. Lin, A. Bansil, D. Grauer, Y. S. Hor, R. J. Cava, and M. Z. Hasan, "Observation of a large-gap topological-insulator class with a single Dirac cone on the surface," Nat. Phys. **5**, 398–402 (2009).
[6]M. Z. Hasan and C. L. Kane, "Colloquium: Topological insulators," Rev. Mod. Phys. **82**, 3045–3067 (2010).
[7]D. Hsieh, D. Qian, L. Wray, Y. Xia, Y. S. Hor, R. J. Cava, and M. Z. Hasan, "A topological Dirac insulator in a quantum spin Hall phase," Nature **452**, 970–974 (2008).
[8]Y. Yan, Z.-M. Liao, X. Ke, G. Van Tendeloo, Q. Wang, D. Sun, W. Yao, S. Zhou, L. Zhang, H.-C. Wu, and D.-P. Yu, "Topological surface state enhanced photothermoelectric effect in Bi_2Se_3 nanoribbons," Nano Lett. **14**, 4389–4394 (2014).
[9]A. Sharma, B. Bhattacharyya, A. K. Srivastava, T. D. Senguttuvan, and S. Husale, "High performance broadband photodetector using fabricated nanowires of bismuth selenide," Sci. Rep. **6**, 19138 (2016).
[10]S. D. Ganichev and W. Prettl, "Spin photocurrents in quantum wells," J. Phys.: Condens. Matter **15**, R935–R983 (2003).
[11]J. W. McIver, D. C. Hsieh, H. Steinberg, P. Jarillo-Herrero, and N. Gedik, "Control over topological insulator photocurrents with light polarization," Nat. Nanotechnol. **7**, 96–100 (2012).
[12]C. Kastl, C. Karnetzky, H. Karl, and A. W. Holleitner, "Ultrafast helicity control of surface currents in topological insulators with near-unity fidelity," Nat. Commun. **6**, 6617 (2015).
[13]P. Seifert, K. Vaklinova, K. Kern, M. Burghard, and A. Holleitner, "Surface state-dominated photoconduction and THz generation in topological Bi_2Te_2Se nanowires," Nano Lett. **17**, 973–979 (2017).
[14]N. Meyer, K. Geishendorf, J. Walowski, A. Thomas, and M. Münzenberg, "Photocurrent measurements in topological insulator Bi_2Se_3 nanowires," Appl. Phys. Lett. **116**, 172402 (2020).
[15]H. S. Shin, B. Hamdou, H. Reith, H. Osterhage, J. Gooth, C. Damm, B. Rellinghaus, E. Pippel, and K. Nielsch, "The surface-to-volume ratio: A key parameter in the thermoelectric transport of topological insulator Bi_2Se_3 nanowires," Nanoscale **8**, 13552–13557 (2016).
[16]J. Gooth, J. G. Gluschke, R. Zierold, M. Leijnse, H. Linke, and K. Nielsch, "Thermoelectric performance of classical topological insulator nanowires," Semicond. Sci. Technol. **30**, 015015 (2015).
[17]V. A. Shalygin, H. Diehl, C. Hoffmann, S. N. Danilov, T. Herrle, S. A. Tarasenko, D. Schuh, C. Gerl, W. Wegscheider, W. Prettl, and S. D. Ganichev, "Spin photocurrents and the circular photon drag effect in (110)-grown quantum well structures," JETP Lett. **84**, 570–576 (2007).
[18]H. Takeno, S. Saito, and K. Mizoguchi, "Optical control of spin-polarized photocurrent in topological insulator thin films," Sci. Rep. **8**, 15392 (2018).
[19]K. N. Okada, N. Ogawa, R. Yoshimi, A. Tsukazaki, K. S. Takahashi, M. Kawasaki, and Y. Tokura, "Enhanced photogalvanic current in topological insulators via fermi energy tuning," Phys. Rev. B **93**, 081403 (2016).
[20]H. Plank, S. N. Danilov, V. V. Bel'kov, V. A. Shalygin, J. Kampmeier, M. Lanius, G. Mussler, D. Grützmacher, and S. D. Ganichev, "Opto-electronic characterization of three dimensional topological insulators," J. Appl. Phys. **120**, 165301 (2016).
[21]L. Braun, G. Mussler, A. Hruban, M. Konczykowski, T. Schumann, M. Wolf, M. Münzenberg, L. Perfetti, and T. Kampfrath, "Ultrafast photocurrents at the surface of the three-dimensional topological insulator Bi_2Se_3," Nat. Commun. **7**, 2041–1723 (2016).
[22]S. Luo, L. He, and M. Li, "Spin-momentum locked interaction between guided photons and surface electrons in topological insulators," Nat. Commun. **8**, 2141 (2017).
[23]P. Olbrich, L. E. Golub, T. Herrmann, S. N. Danilov, H. Plank, V. V. Bel'kov, G. Mussler, C. Weyrich, C. M. Schneider, J. Kampmeier, D. Grützmacher, L. Plucinski, M. Eschbach, and S. D. Ganichev, "Room-temperature high-frequency transport of Dirac fermions in epitaxially grown Sb_2Te_3- and Bi_2Te_3- based topological insulators," Phys. Rev. Lett. **113**, 096601 (2014).
[24]H. Plank, L. E. Golub, S. Bauer, V. V. Bel'kov, T. Herrmann, P. Olbrich, M. Eschbach, L. Plucinski, C. M. Schneider, J. Kampmeier, M. Lanius, G. Mussler, D. Grützmacher, and S. D. Ganichev, "Photon drag effect in $(Bi_{1-x}Sb_x)_2Te_3$ three-dimensional topological insulators," Phys. Rev. B **93**, 125434 (2016).
[25]T. Schumann, N. Meyer, G. Mussler, J. Kampmeier, D. Grützmacher, E. Schmoranzerova, L. Braun, T. Kampfrath, J. Walowski, and M. Münzenberg, "Observation of spin Nernst photocurrents in topological insulators," arXiv:1810.12799 (2018).

Supplementary Material: The impact of metallic contacts on spin-polarized photocurrents in topological insulator Bi_2Se_3 nanowires

N. Meyer,[1, a)] K. Geishendorf,[2] J. Walowski,[1] A. Thomas,[2] and M. Münzenberg[1]

[1)] *Institute of Physics, University of Greifswald, Felix-Hausdorff-Str. 6, 17489 Greifswald, Germany*

[2)] *IFW Dresden, Institute for Metallic Materials, Helmholtzstraße 20, 01069 Dresden, Germany*

The position dependence of the thermovoltage can be described by a two-interface Seebeck model. The device can be simplified to a combination of two metal contacts connected by one nanowire and in contact with a voltmeter. We omit the 5 nm thick chromium interlayer and treat the contacts as pure gold layers. The thermovoltage ΔV measured between the two metal contacts is then given by

$$\Delta V = V_D - V_s = (S_{Au} - S_{TI})(T_D - T_S) \tag{1}$$

where S_{Au} is the Seebeck coefficient of the gold contact, S_{TI} is nanowire Seebeck coefficient, T_D is the drain temperature (ground electrode), and T_S is the source temperature (minus pole). We have $S_{Au} - S_{TI} > 0$ in Eq.(1), since the Seebeck coefficient for gold is $S_{Au} = 1.94\,\mu V/K$ at 300 K and for Bi_2Se_3 nanowires is $S_{TI} \approx 100\,\mu V/K$ at 300 K[1]. When the drain electrode is illuminated, we get $T_D > T_S$ which results in a positive thermovoltage ΔV. This is in good agreement with FIG. 3(d) in the main manuscript. Illuminating the source electrode would reverse the voltage which matches the results in FIG. 3(d). Changing the contact geometry from axisymmteric to point-symmetric (see FIG. 3(a) in the main manuscript) does not effect the temperature gradient. Hence, the results in FIG. 3(a) and (f) are the same. Since the temperature difference $T_D - T_S$ changes linear with the laser spot position, the thermovoltage in Eq. (1) should also depend linearly on the laser spot position. Thus, the two-interface Seebeck effect in Eq. (1) can explains the linear region of the contour plot in FIG. 3(a) and (d) but not the enhancement at the nanowire/contact intersection.

[1]H. S. Shin, B. Hamdou, H. Reith, H. Osterhage, J. Gooth, C. Damm, B. Rellinghaus, E. Pippel, and K. Nielsch, "The surface-to-volume ratio: a key parameter in the thermoelectric transport of topological insulator Bi_2Se_3 nanowires," Nanoscale **8**, 13552–13557 (2016).

[a)]Electronic mail: nina.meyer@uni-greifswald.de; corresponding author

3.4 Observation of spin Nernst photocurrents in topological insulators

Observation of spin Nernst photocurrents in topological insulators

[1]T. Schumann, [1]N. Meyer, [2]G. Mussler, [2]J. Kampmeier, [2]D. Grützmacher,[3]E. Schmoranzerova, [4]L. Braun, [4]T. Kampfrath, [1]J. Walowski, [1]M. Münzenberg

1. *Institut für Physik, Universität Greifswald, Felix-Hausdorff-Straße 6, 17489 Greifswald, Germany*
2. *Peter Grünberg Institut (PGI-9) and Jülich-Aachen Research Alliance (JARA-FIT), Forschungszentrum Jülich, 52425 Jülich, Germany*
3. *Department of Chemical Physics and Optics, Charles University, Ke Karlovu 3, 121 16 Prague, Czech Republic*
4. *Department of Physical Chemistry, Fritz Haber Institute, Faradayweg 4-6, 14195 Berlin, Germany*

Abstract: The theoretical prediction of topological insulators in 2007 triggered tremendous interest. A major reason is their topological twist in reciprocal space, which comes along with unidirectional, spin-polarized surface-state currents. This property makes topological insulators on one hand perfectly suited materials for optically generated, ultrafast spin-current bunches. On the other hand, those spin-polarized surface-state currents, when generated by a voltage, lead to large spin Hall effects, or when generated by a temperature gradient, result in the thermal analogue, the spin Nernst effect. Both effects mutually convert charge/heat currents into transverse spin currents, thereby leading to spin accumulation. By connecting thermal and optical effects through a local laser excitation, we observe signatures of heat-transport related spin Hall effects that can be extracted from opto-transport experiments. We detect the heat-driven spin Nernst effect that drives a transverse spin-current and results in a spin accumulation at the topological insulator edges. The circular photo-galvanic current, three orders of magnitudes smaller than the thermal currents, allows one to map the spin distribution via its strong sensitivity to the circular polarization dependence in the optical transitions. We illuminate the detailed thermocurrent distribution, including the influence of edges and contacts, in spatially resolved current maps. This opens up new ways for spin detection and generation in topological insulators.

A three-dimensional topological insulator (3D-TI) is a material with strong spin-orbit interaction that gives rise to surface states with specific properties [1, 2, 3, 4, 5]. One of the most prominent is that, in contrast to the insulating bulk of the material, the surface states display a metal-like conductivity [6]. Furthermore, the surface states show a distinct spin texture that connects the direction of the carrier spin to its momentum (spin-momentum locking). Recently, large effort has been aimed at using the spin-momentum locking for generation of charge currents with a large degree of spin polarization, pure spin currents, or to control a charge current direction in the surface channel [7]. In a

seminal work [4], this effect was applied to excite a helicity-dependent photocurrent at the sample surface at room temperature [4, 8, 9].
Different effects of thermal origin can influence the transport in these materials, affecting the helicity-dependent signals. Therefore, it is crucial to understand the origin of each contribution to the photocurrent and their underlying microscopic mechanisms. The relative complexity of the photocurrent behavior arises from the broad energy regime of the optical excitation used in the seminal studies. The prototype 3D-TI materials are chalcogenides such as Bi_2Se_3, Bi_2Te_3 or Sb_2Te_3 [1, 3]. From the intensive materials exploration and studies of photoemission over the last years, it is possible to gain control over their band structure and the gap crossing Dirac cone. All of them are narrow-gap semiconductors and have bulk band gaps in the range of 200 – 300 meV. Their Fermi level position can be adjusted over a wide range, in alloys such as $(Bi,Sb)_2Te_3$, resulting in very low carrier concentrations and low intrinsic conduction of the bulk material [10].
The band gap is very narrow with respect to optical applications. The excited states are found within the Dirac cone only for excitation wavelengths larger than 4 μm. However, typical photon energies used in optical experiments are in the visible and near infrared (NIR) region, at around 0.8 μm, and the photon energies are five to eight times the value of the bulk band gap. Therefore, the surface states in the Dirac cone are excited far into the bulk valence band. This gives rise to a whole variety of optically induced effects. Depending on the time scales relevant for the effect under study, two types of experiments are performed, (i) the ultrafast photocurrent generated in the dynamic regime by femtosecond laser pulses, which allows one to separate the different time scales of charge and spin relaxation, and (ii) quasi-equilibrium carrier transport by continuous wave excitation, typically performed in a form of an opto-electrical measurement on micro patterned devices [7].

The ultrafast spin and carrier dynamics has been successfully investigated in many types of time-resolved optical experiments, by direct detection of helicity dependent polarization in films using magneto-optics [11], by THz emission [12] or by electric sampling using amorphous Silicon-Auston switches [9, 13]. In our previous work [11], we used the all-optical pump-probe technique to examine the coherent ultrafast spin-dynamics of $(Bi,Sb)_2Te_3$ (BST) alloys. The electrons are excited into the second Dirac cone [14] and subsequently relax towards the bottom of the conduction band [15]. The spin polarization of the electrons at the moment of excitation is given by the energy and polarization of the absorbed photon. One finds spin-dependent photogalvanic effects arising from spin-orbit interaction in non-centrosymmetric materials [16], and the photon

drag effect [17] or [18] arising from a band-dependent speed of the charge carriers. These effects result in spin-polarized currents in a semiconductor after optical excitation.
All the above-mentioned phenomena can be of importance with respect to the quasi-equilibrium photocurrents detected in transport experiments, and respectively have an impact on the photocurrents. Recently, in the work by Pan et al. [19], these phenomena were disentangled by studying photocurrents over a large wavelength range, combined with a modification of the electrochemical potential by a gate voltage. Apparently, the photocurrents can have also a complex spatial dependence. Substrate effects can contribute, as well as the depth dependent photo-Dember effects, which is a typical source of ultrafast spin currents in semiconductors [5]. At the contacts, a spatial inhomogeneity of the induced photocurrents is expected. The origin of this inhomogeneity can be manifold, for example the modification of the local potential landscape at metal/semiconductor interface and the formation of a Schottky barrier. This has been demonstrated for ultrafast photocurrents in graphene nanojunctions [20, 13]. Therefore, in our work, we want to discuss the lateral effects by looking in detail into their spatial dependence along the Hall bar.

Our approach also establishes another way to create spin-polarization by sending a current though a thin film in a per se nonmagnetic material. The spin Hall effect converts a longitudinal charge current in the bulk of the material into a transverse spin current. The efficiency is given by the so called spin Hall angle $\theta_{Spin\ Hall} = \frac{|J_{spin}|}{|J_{charge}|}$ [7]. The spin Hall effect is exploited in heavy metals [7, 21] to create large spin orbit torque at interfaces in ferromagnet bilayers [22, 23]. A search for increasing the efficiency is ongoing. So far, the spin Hall angle $\theta_{Spin\ Hall}$ is far below one in these materials, typically about 0.1 – 0.3. For ferromagnet/topological insulator heterostructures, in contrast, very high spin orbit torque efficiencies have been reported recently [24, 25, 26, 27, 28].
The hallmark of topological insulators is the large intrinsic spin-orbit interaction, resulting in much higher charge-to-spin conversion than in heavy metals. Huge factors of $\theta_{Spin\ Hall}$ have been observed in structures with magnetically doped TIs [24], and even values of >18 for sputtered granular topological insulator films [25]. One explanation is that those large values result from the definition of $\theta_{Spin\ Hall}$. A large resistance of the bulk of TIs compared to metals, makes the denominator in $\theta_{Spin\ Hall}$ close to zero, increasing the value of $\theta_{Spin\ Hall}$. This shows the relevance of a detailed understanding of the mechanisms leading to the extreme spin orbit torque switching efficiency [24, 25, 26].

The spin Hall effect has a thermal analogue, the spin Nernst effect. A longitudinal heat current in the material drives a transverse spin current. Microscopically, it originates from an interplay of temperature driven electrons, feeling locally spin-orbit effects in the material. This effect has been only recently discovered in Pt [29] but not yet in topological insulators. We want to understand how light-generated effects, instead of voltage-generated currents, interact with surface currents in topological insulators. Light acts in two ways on the topological insulators film, it creates (i) a photo-excitation of the carriers and (ii) a heat gradient. The question is whether we can drive a spin Hall effect by light to accumulate spins.
In this work, we aim to combine the spin Hall effect physics in topological insulators, with the optical excitation of the materials in terms of a spin Hall photoconductance [30]. We report on the appearance of a spin Nernst effect-like contribution to the photocurrent in a Hall bar. We attribute this signal to a spin accumulation originating from a spin-orbit driven transverse spin-current, as a response to the longitudinal thermocurrent, which is detected via a helicity-dependent photocurrent modified by the spin accumulation.

For the photoelectric measurements, we use a well-established lock-in technique. The light source is a diode laser with a wavelength of 785 nm (1.55 eV) modulated at 77Hz by a square-function generator. In our experiments, laser radiation is focused down to a 3 μm wide beam on the sample surface. In this slow regime, the photo-response mirrors the quasi static rectangular excitation pattern, and at the same time excludes dynamic effects, which occur at higher modulation frequencies. The setup allows precise laser spot positioning by stepper motors, with high axial and lateral resolutions down to 200 nm along the sample surface, while measuring the reflectivity and the voltages generated by the photocurrents.

We have developed a method to map the contributions to the generated voltage for each point spatially and as a function of the polarization of light. For this purpose, at each point, the reflectivity and the photovoltage V_{photo} generated by the thermocurrent, excited by the laser beam, is recorded for a full rotation of the quarter-wave plate (λ/4plate). We use the same analysis, as proposed by Ganichev in reference [17] for the analysis of spin photogalvanic effects in GaAs, and which was also used by McIver et al. in reference [4] for the study of topological insulators. We fit each point by the following equation:

$$V_{\mathrm{photo}}(\theta) = C \cdot \sin(2\theta) + L_1 \cdot \sin(4\theta) + L_2 \cdot \cos(4\theta) + D \qquad (1)$$

The angle θ denotes the rotation angle of the λ/4 plate around the light propagation axis in a perpendicular plane for each single measurement, as depicted in Fig. 1. When rotating the λ/4 plate, the light polarization changes from linear polarized photons for 0°, 90°, 180° and 270° to right-circular for 45°, 225° and left-circular for 135°, 315° polarized light.
Equation (1) reflects the voltage contributions of various periodicity with respect to the angle θ, i.e. polarization variation. The factor D gives the polarization-independent voltage. It includes the Seebeck voltage generated by heat gradients driven by the laser. The coefficients L_1 and L_2 capture the weight of the components with period 4Θ, and they are 90° out of phase relative to each other. They depend on the angular alignment of the incident light, its polarization relative to the samples surface in general, and especially to crystalline axes of the material. Therefore, both L_1 and L_2 potentially address multiple effects connected to the linear polarization axis, which consist of common effects like polarization sensitive absorption, changing effectively the heat gradient, and less common effects like a photon drag effect [18].
The factor C weighting the component with 2Θ, represents the contribution of interest here: it originates from a circularly polarization-driven photocurrent, e.g. the difference in photocurrent for right- and left-circularly polarized light. In the common interpretation, the circularly polarized light promotes the excitation of one spin species (spin up or down), respectively. It generates a directional current which originates from the spin imbalance, the asymmetrically populated surface states in k-space in conjunction with spin-momentum locking in the topological insulator, resulting in a directional current on the surface. The process is called circular photogalvanic effect. To avoid the experiments being affected by dichroic absorption effects that would also modify the factor C amplitude, we measure the reflectivity and photocurrents at the same time for a full rotation cycle. These two-dimensional power absorption and reflectivity maps allow determining the influence of local heating by the scanning laser spot. Since the absorption is polarization-dependent by itself, this is a precondition to interpret the background of Seebeck voltage that contributes in addition to the polarization dependence.
Fig. 1a shows a sketch of the setup with an optical microscope image of the sample and the sample geometry. The angle of incidence of the laser beam is kept fixed at 45° to the sample normal. In Fig. 1b, a reflectivity map of the sample area is depicted, taken simultaneously with the voltage map. The Au contacts show the highest reflection in white. The substrate appears almost black on the scale (low reflectivity signal), and the topological insulator is grey in between. These reflectivity and V_{photo} maps are also

compared for s- and p- polarization in detail in the section below. Thereby, we thoroughly analyze possible edge absorption effects. We find them to be minor for these local measurements.

In the following discussion, we have chosen a $(Bi_{0.57}Sb_{0.43})_2Te_3$ ternary heterostructure (BST) with a total thickness of 16 nm. BSTs allow the tuning of the Fermi level between valence and conduction band, based on the bismuth to antimony ratio, especially as close as possible to the Dirac point [10]. In addition, this doping in the band gap minimizes the concentration of mobile charge carriers in the thin film. The minimum charge carrier concentration of $3 \cdot 10^{13}$ cm^{-2} is determined by transport measurements. The ternary $(Bi_{0.57}Sb_{0.43})_2Te_3$ alloy is grown by molecular-beam epitaxy [31, 32] on a Si-(111) surface, which is the uppermost layer of the silicon-on-insulator (SOI) substrate. The BSTs are analyzed by various experiments, including x-ray photoelectron spectroscopy (XPS), x-ray diffraction (XRD), Raman spectroscopy, angular resolved photo electron spectroscopy (ARPES). ARPES monitors the Fermi level movement through the band gap by regulating the antimony amount, which is also confirmed by the corresponding Hall effect mapping of the n- to p-type doping transition. Our samples are chosen to be located very close to this compensation point with the lowest intrinsic conductance. After structuring the thin films into Hall-bars by optical lithography and Ar^+-ion dry etching they are stored under dry vacuum conditions. This surface-reconstruction procedure is verified by ARPES measurements to yield the correct surface states and Fermi level again.

Large-scale overview maps are performed on the Hall bar devices to analyze the role of the contacts and substrate on the photocurrents. The data is presented in Fig. 1c and d. Each point of these maps has been analyzed by equation (1) to extract the parameters D, L_1, L_2 and C. The thermovoltage (D) and the photogalvanic voltage (C) are displayed, respectively. The contacts on the right side are used during the experiment to pick up the signals in between. It can be seen that the largest polarization-independent voltages appear when the laser spot excites the media right at the structured contacts, but also finite and non-trivial dependencies along the topological insulator structure are found.

The thermovoltage D reverses the sign at each contact, and the signal strength is of the size of a few mV at the contacts. Elsewhere, they are mainly on the order of hundreds μV. These thermovoltage distributions can be explained by the lateral variations of the reflectance, shown in Fig. 1b. The largest values of D are found in particular at the topological insulator-substrate interface close to the contacts. Almost no thermovoltage is found for the excitation on top of the Au metal contact, where the highest reflectance

occurs. These voltage signals show a sign reversal for the doping of the topological insulator going from n- to p-type, which is expected.
The focus of our study is the search for the signal component which is sensitive to the exciting photon's helicity, associated with the circular photogalvanic voltage (parameter C in equation (1)). These signals are at least a factor of hundred smaller in amplitude compared to parameter D, associated to the thermocurrent, making their extraction generally challenging. In the large overview map, we see that with moving the excitation laterally, abrupt changes from +5 to -5 μV for C can appear, for substrate to topological insulator edges close to the contacts. We tested s- and p-polarized light, photocurrent maps in overview maps and in detail in the Hall bar center for significant changes at edges or other potential sensitive regions (e.g. plasmonic effects). However, these changes turn out to be negligible and will not be discussed in the following. The spatial irregular distribution of the values for C tells us that no meaningful values can be extracted in the large overview scans for the dichroic shift currents.

In order to extract meaningful values for each parameter, photocurrent scans with higher spatial resolution are required. Fig. 2 shows measurements, focused on the geometrical center of the Hall bar device between two contacts, using a higher spatial resolution. Again, we discuss the extracted values for C and D. Example fits of equation (1) are shown for three positions 1-3 in Fig. 2. This position is chosen to reduce the thermocurrent. Its minimum is expected in the geometrical center between the contacts. Consequently, the non-thermal contribution to signals driven by the circular polarization driven photocurrent will be dominant. This idea is similar to the concept used by McIver et al. [4] previously.
The 2D map in Fig. 3 in the upper left shows the thermocurrent distribution for the chosen region. For all points, the average thermovoltage is positive and in the order of 125 μV, indicated by the red color scale over the full scan range. Again, for a more detailed discussion, averaged profiles consisting of multiple lines of a section of the data area, are shown parallel and perpendicular to the Hall bar, to the top and right side of the color plot (Fig. 3): The marked regions are two perpendicular lateral profiles, where we identify a monotonic drop of the D value along the Hall bar. This is expected when moving the laser spot between contacts. However, although there is a linear dependence due to a thermovoltage offset on the BST Hall bar, the data shows no zero crossing. Since the values of L_1 and L_2 go with the sine and cosine of 4Θ, the complex L-value ($L=L_1+iL_2$) can be plotted as modulus and its phase. For the modulus we find values about a factor of ten smaller than D. The phase change is the strongest for s- and p-polarization, as shown in Fig. 5. For C values extracted from the fits at each point of the

scan regions, we find that the circular photogalvanic effect is again a factor of hundred smaller, in the μV range. The most important finding of this section is that there is a unidirectional offset thermovoltage present on the BST Hall bar, which indicates the existence of a temperature gradient ∇T directed along the Hall bar device.

The unexpected findings are presented in Fig. 3, where a spatially resolved map of the C-value, originating from the difference in photovoltages for the right- and left-handed circularly polarized laser excitation is shown in a false-color plot. In the middle region, the C-values stay almost constant along the bar, which is contrary to the thermovoltage. In addition, a complex behavior occurs at the edges of the Hall bar. There, the voltage reverses direction, as indicated by the blue and red areas at both edges. This resembles immediately a spin-Hall-like signal in the Hall-bar structure. In the profile line, these are more visible as local maxima and minima. We find an asymmetry of our photocurrent with respect to the polarization of the light for right- or left-handed circular polarization. The spins generated by the selective excitation by the circularly polarized light generate a positive or negative voltage depending on their polarization.

What is the origin of this signal that resembles a spin accumulation at the edges, measured by the excitation difference for the two polarizations? Recently, related findings of a spin-Hall photoconductance effect were reported by Seifert et al. [30]. They observed that at the edges of Bi_2Te_2Se platelets, spin accumulation modified by the photoconductance occurs. By varying the driving current, they tested different symmetry scenarios and deduced that the accumulation of spins at the edges arises from the spin-Hall effect in the topological insulator bulk states. Further, they found that the spin accumulation at the edges gives rise to an optically induced kind of magnetoresistance effect, e.g. a change of the edge channel photoconductance that is connected to the spin-population and the light's circular polarization. Here, we observe a similar signature, but without any application of an external current.
The microscopic process is depicted in Fig. 4 schematically: instead of a voltage driving the transverse spin current, we observe a thermal gradient driving a transverse spin accumulation at the edges via the spin Nernst effect, the thermal analogue to the spin Hall effect [29]. This thermally driven spin polarization changes the weighting in the spin population, sensed by the exciting photon helicity. Thus, the laser light action is twofold: The laser generates the heat gradient and the spins accumulated at the device edges, determined by the size of the spin Nernst effect. Additionally the size of the circular photogalvanic effect itself depends on the helicity-dependent photoexcitation of the carriers. The latter appears as a contrast in the spin-voltage maps of the C value that

originates from current direction J_C of the carriers excited selectively by circularly polarized photons reversing sign for left and right circularly polarized light. It senses the accumulated spins at the device edges, and, thus, the spin density accumulated at the edges can be accessed. It seems that we have here a very sensitive method that allows to detect a voltage on top of a three orders of magnitude larger Seebeck voltage. Recently, we have shown that this method can be applied even for more complex nanoscale geometries and topological insulator nanowires [33, 34] and ferromagnet/ topological hybrid structures.

We have presented a study of the photoexcitation in the three-dimensional topological insulator $(Bi_{0.57}Sb_{0.43})_2Te_3$ with a fixed intrinsic doping level leading to the lowest intrinsic conduction of the bulk states. For the thin-film geometry, the Hall-bar device is studied in an overview map of the polarization-dependent photocurrents to elucidate the effects especially of the contacts, revealing an offset Seebeck voltage along the Hall bar. The high-resolution map shows a contrast of the device at the edges that have the signature of the spin Nernst effect. We interpret this signal as a transverse spin current driven by the thermal gradient along the Hall bar. The resulting spin accumulation influences the spin-dependent circular photogalvanic effect that allows detecting a difference in the spin accumulation via the polarization-dependent photovoltage signal. This opens up new possibilities to exploit the spin-polarization created by thermal gradients and to use the sensitive detection by light-induced effects to study the processes. We present a contact free way to generate local spin-accumulation in topological insulators which might be useful for spintronic applications, magnetoresistance effects and spin torques in topological materials.

Acknowledgements

We acknowledge funding through the Deutsche Forschungsgemeinschaft (DFG) via the priority program, SPP "Topological Insulators: Materials - Fundamental Properties - Devices“ (SPP 1666) and DAAD-PPP Czech Republic, project “FemtomagTopo”. E.S acknowledges “INTER-COST grant no. LTC20026”. We thank the fruitful discussions with A. Holleitner.

Author contributions

M.M. and E.S. designed the experiment. T.S., N.M., J.W., E.S., developed the interfaces to measure and analyze the experimental data and carried out the photocurrent

experiments. M.M., T.S., J.W. and E.S. developed the model. G.M., J.K., and D.G. prepared and characterized the samples. T.S., N.M., G.M., J.K., D.G., L.B., T.K., J.W. and M.M. discussed the data and interpretation. T.S., E.S., G.M., J.W. and M.M wrote the manuscript. All the authors reviewed and discussed the manuscript.

Figures:

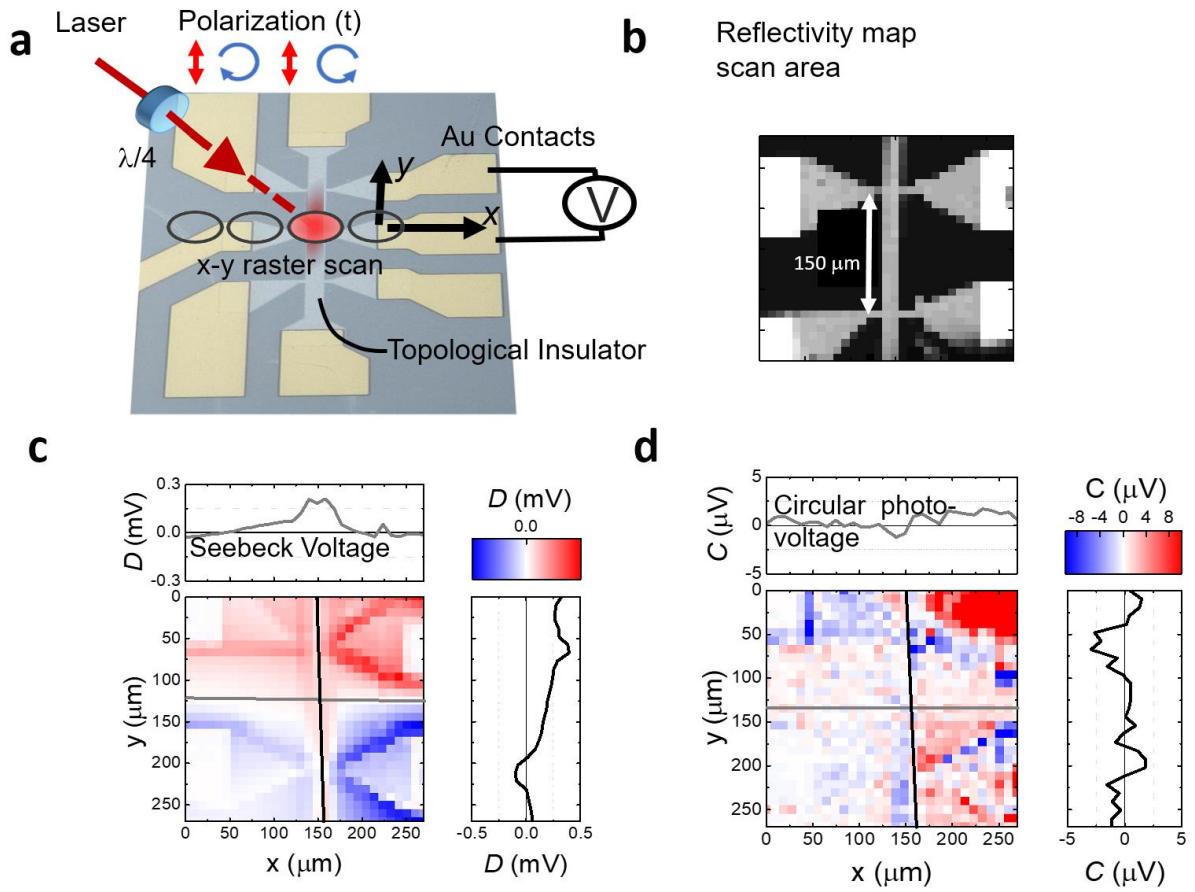

Fig. 1| Experimental setup. a, Schematic layout of the topological insulator sample structure with intrinsic doping (16 nm $(Bi_{0.57}Sb_{0.43})_2Te_3$) and measurement alignment. The x-y-scanning laser excitation relies on piezo-driven motion of the sample while measuring the voltage (not to scale). For each point, the laser polarization is varied from linear to right- to linear to left-handed circularly polarized using a λ/4-wave plate. The Au contact pads are the golden leads, and the topological insulator Hall bar structure is seen in lighter gray on the darker grey silicon substrate in the optical microscope image. **b,** A reflectivity map derived from scanning the sample in x and y direction showing the closeup of the investigated 150 µm long Hall-bar region. **c,** The coefficient D, assigned to the Seebeck thermovoltage, is plotted as false-color plot. **d,** The coefficient C represents the circular photogalvanic voltage and is plotted in a false-color plot. The graphs show the detailed profile sections along the Hall bar (black line) and perpendicular (gray line) at the side and top.

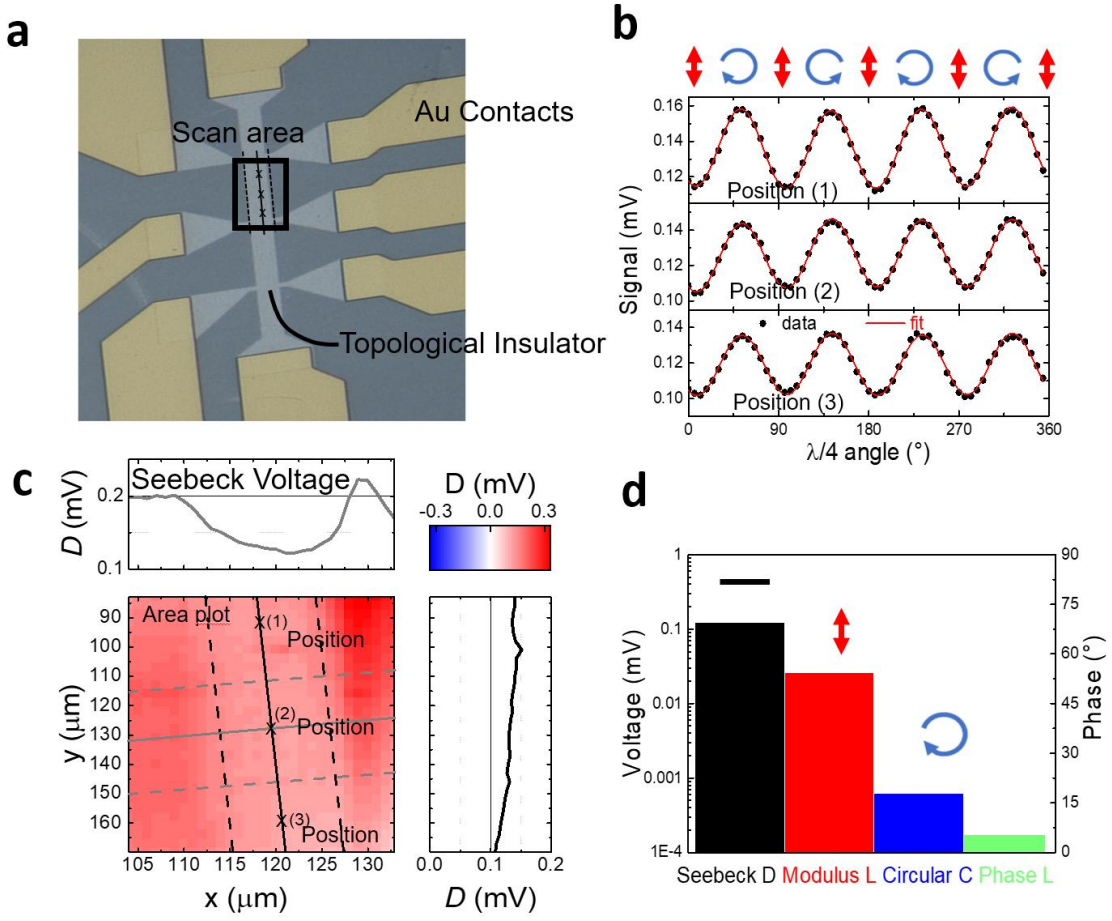

Fig. 2| Detailed measurements and photogalvanic-effect analysis. a, The Au contact pads are the Au leads, and the topological-insulator Hall-bar structure is seen in lighter gray on the darker grey silicon substrate in the optical micrograph. The x-y-laser-scanned area is marked. **b,** and **c,** Map showing the thermovoltage parameter D (Seebeck voltage) for the topological-insulator Hall bar. The graphs show the detailed profile sections along the Hall bar (black line) and perpendicular (gray line). For each specific position (1), (2) and (3), the laser polarization is scanned from linear to right- to linear to left-handed circularly polarized using a λ/4-wave plate. For the polarization-dependent signal (black dots) for the λ/4-plate rotation angle θ is plotted together with fits using equation (1). **d,** The parameters D, L_1, L_2 and C (for modulus and phase of $L=L_1+iL_2$) for position (3) are shown in the bar diagram.

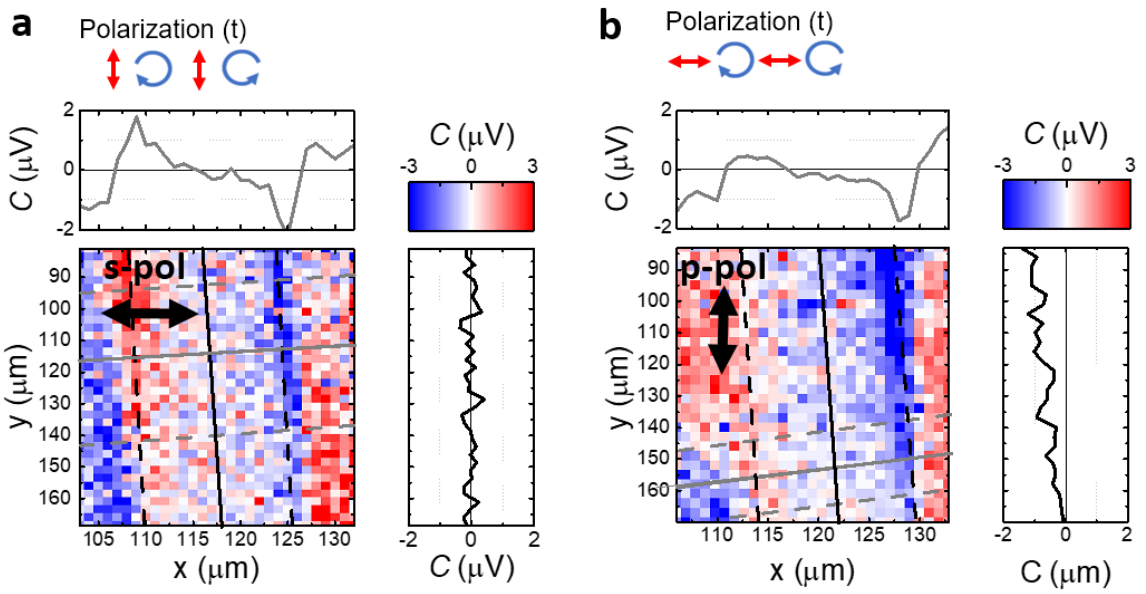

Fig. 3| Interplay between the thermocurrent offset and circular photogalvanic voltage signal. Comparison of two optical excitation scenarios. The panel shows parameter C, the voltage generated by the circular photogalvanic effect, created by the circular polarized light for both scenarios. The incident laser beam is **a,** s-polarized and **b,** p-polarized, respectively to discuss the effect of the linear polarization interacting with the Hall bar edges. The general feature of the strong voltage signal at the edges in the circular photogalvanic effect, positive and negative, respectively, is not altered.

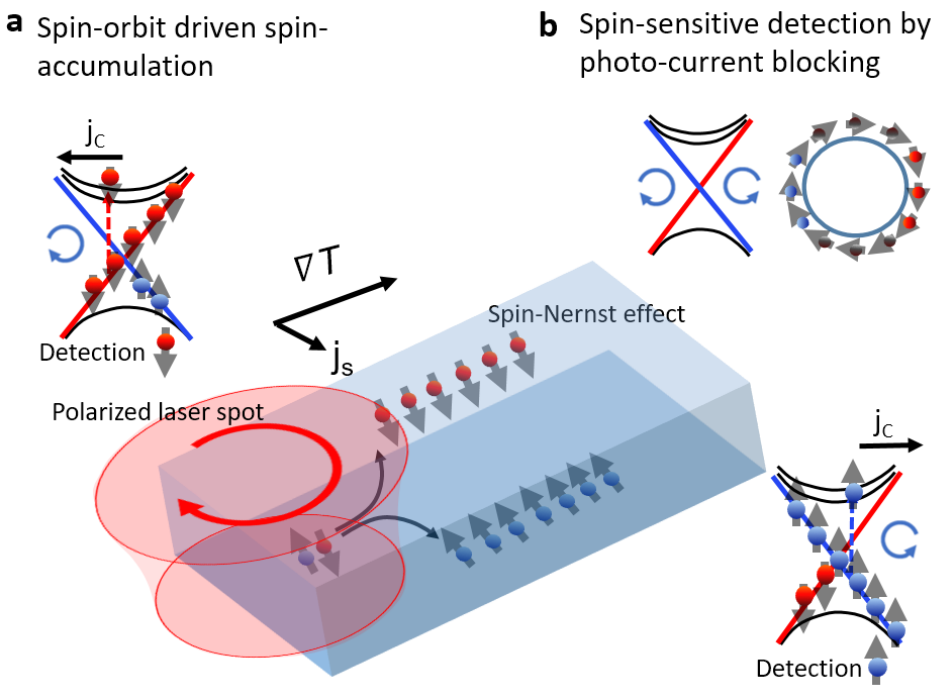

Fig. 4| Spin accumulation and spin-sensitive detection. The model explains the two-step spin-accumulation process. First, the spin Nernst effect accumulates the spins towards the edges of the bar, perpendicular to the temperature gradient ∇T. This spin-current j_s results in a steady-state modification of spin at around the Dirac cone at the topological insulator edges. By scanning the laser beam using polarization modulation, spin-sensitivity comes into play: the altered spin occupation modifies the circular photogalvanic current, three orders of magnitude smaller than the Seebeck currents. This sensitive selection by the circular right (left side) and left (right side) polarized photons results in a modification of the circular photogalvanic current j_C that allows to map and detect this local spatial spin imbalance driven by the spin Nernst effect in the circular photogalvanic voltage C driven by the photocurrent j_C. Due to the symmetry breaking by the contacts, an overall temperature gradient is found along the Hall bar with x-y-scanning of the laser spot (see Fig. 2c).

References

[1] Fu, L., Kane, C. L. & Mele, E. J. Topological insulators in three dimensions. *Phys. Rev. Lett.* ***98***, 106803 (2007).

[2] Ando, Y. Topological Insulator Materials. *J. Phys. Soc. Jpn.* ***82***, 102001 (2013).

[3] Hasan, M. Z. & Kane, C. L. Colloquium: Topological insulators. *Rev. Mod. Phys.* **82**, 3045-67, (2010).

[4] McIver, J. W., Hsieh, D., Steinberg, H., Jarillo-Herrero, P., & Gedik, N. Control over topological insulator photocurrents with light polarization. *Nature Nanotech.* ***7***, 96-100 (2011).

[5] Braun, L. *et al.* Ultrafast photocurrents at the surface of the three-dimensional topological insulator Bi_2Se_3. *Nature Comm.* **7**, 13259 (2016).

[6] Sinova, J. *et al.* Universal intrinsic spin Hall effect. *Phys. Rev. Lett.* **92**, 126603 (2004).

[7] Sinova, J., Valenzuela, S. O., Wunderlich, J., Back, C. H. & Jungwirth, T. Spin Hall effects. *Rev. Mod. Phys.* **87**, 1213-60 (2015.)

[8] Hsieh, D., *et al.* Selective probing of photoinduced charge and spin dynamics in the bulk and surface of a topological insulator," *Phys. Rev. Lett.* 107, 77401 (2011).

[9] Kastl, C., Karnetzky, C., Karl, H. & Holleitner, A. W. Ultrafast helicity control of surface currents in topological insulators with near-unity filelity. *Nature Comm.* **6**, 6617 (2015).

[10] Kellner, J., *et al.* Tuning the Dirac point to the Fermi level in the ternary topological insulator $(Bi_{1-x}Sb_x)_2Te_3$. *Appl. Phys. Lett.* **107**, 251603 (2015).

[11] Boschini, F. *et al.* Coherent ultrafast spin-dynamics probed in three dimensional topological insulators. *Sci. Rep.* **5**, 15304 (2015).

[12] Seifert, T. *et al.* Efficient metallic spintronic emitters of ultrabroadband terahertz radiation. *Nature Photon* **10**, 483-8 (2016).

[13] Brenneis, A. *et al.* THz-circuits driven by photo-thermoelectric, gat-tunable graphene-junctions. *Sci. Rep.* **6**, 35654 (2016).

[14] Sobota, J. A. *et al.* Direct optical coupling to an unoccupied dirac surface state in the topological insulators Bi_2Se_3. *Phys. Rev. Lett.* **111**, 136802 (2013).

[15] Myung-Soo, L. & Seung-Hoon, J. Thermoelectric properties of thin film topological insulators: A first-principles study. *Solid State Comm.* **270**, 22-5 (2017).

[16] Ganichev, S. D. *et al.* Spin-galvanic effect *Nature* **417**, 153-6 (2002).

[17] Ganichev, S. D. & Prettl, W. Spin photocurrents in quantum wells: Topological Review. *J.Phys.:Condens. Matter* **15**, R935-R983 (2003).

[18] Plank, H. *et al.* Photon drag effect in $(Bi_{1-x}Sb_x)_2Te_3$ three-dimensional topological insulator. *Phys. Rev. B* **93**, 46 (2016).

[19] Pan, Y. *et al.* Helicity dependent electrically gated $(Bi_{1-x}Sb_x)_2Te_3$ thin films. *Nature Comm.* **8**, 1037 (2017).

[20] Obraztsov, P. A. *et al.* All-optical control of ultrafast photocurrents in unbiased graphene. *Sci. Rep.* **4**, 4007, 2014.

[21] Bekele, Z. A. *et al.* Spin-orbit torque induced magnetization switching in heavy metal/ferromagnet multilayers with bilayer of heavy metals. *Solid State Comm.* 262, 44-9 (2017).

[22] Liu, L., Lee, O. J., Gudmundsen, T. J., Ralph, D. C. and Buhrmann, R. A. Current-induced switching of perpendicularly magnetized magnetic layers using spin torque from the spin Hall effect. *Phys. Rev. Lett.* **109**, 096602 (2012).

[23] Miron, I. M. *et al.* Perpendicular switching of a single ferromagnetic layer induced by inplane current injection. *Nature* 476, 180-193 (2011).

[24] Fan, Y. *et al.* Magnetization switching through giant spin-orbit torque in a magnetically doped topological insulator heterostructure. *Nature Mater.* **13**, 699-704 (2014).

[25] Mahendra, D. C. *et al.* Room-temperature perpendicular magnetization switching through giant spin-orbit torque from sputtered $Bi_xSe_{(1-x)}$ topological material. *arXiv:1703.03822* (2017).

[26] Wang, Y. *et al.* Room temperature magnetization switching in topological insulator-ferromagnet heterostructures by spin-orbit torques. *Nature Comm.* 8, 1364 (2017).

[27] Mellnik, A.R. *et al.* Spin-transfer torque generated by a topological insulator. *Nature* **511**, 449-51 (2014).

[28] Nguyen, H. D. K., Yugo, U. & Pham, N. H. A conductive topological insulator with colossal spin Hall effect for ultra-low power spin-orbit-torque switching. *Nature Mater.* **17**, 808–813 (2018).

[29] Meyer, S. *et al.* Observation of the spin Nernst effect" *Nature Mater.* **17**, 977–981 (2017).

[30] Seifert, P. *et al.* Spin Hall photoconductance in 3D Topological Insulator at room temperature. *Nature Comm.* **9**, 331 (2018).

[31] Weyrich, C. *et al.* Growth, characterization and transport properties of ternary $(Bi_{1-x}Sb_x)_2Te_3$ topological insulator layers. *J. Phys.: Condens. Matter* **28**, 495501 (2016).

[32] Krumrain, J. *et al.* MBE growth optimization of topological insulator Bi_2Te_3 films. *J. of Crystal. Growth* 324, 115-118 (2011).

[33] N. Meyer, K. Geishendorf, J. Walowski, A. Thomas, M. Münzenberg, Photocurrent measurements in topological insulator Bi_2Se_3 nanowires, *Appl. Phys. Lett.* **116**, 172402 (2020).

[34] N. Meyer, K. Geishendorf, J. Walowski, A. Thomas, M. Münzenberg, The impact of metallic contacts on thermoelectric and spin-polarized photocurrents in topological insulator Bi_2Se_3 nanowires, *Appl. Phys. Lett.* **117**, 262401 (2020).

4 Eigenständigkeitserklärung

Hiermit erkläre ich, dass diese Arbeit bisher von mir weder an der Mathematisch-Naturwissenschaftlichen Fakultät der Universität Greifswald noch einer anderen wissenschaftlichen Einrichtung zum Zwecke der Promotion eingereicht wurde.
Ferner erkläre ich, dass ich diese Arbeit selbstständig verfasst und keine anderen als die darin angegebenen Hilfsmittel und Hilfen benutzt und keine Textabschnitte eines Dritten ohne Kennzeichnung übernommen habe.

Greifswald, den Nina Meyer

5 Curriculum vitae

6 Scientific contributions

(a) "*Photocurrent measurements on topological insulator Bi_2Se_3 nanowires*"
N. Meyer, K. Geishendorf, J. Walowski, A. Thomas and M. Münzenberg, *Appl. Phys. Lett.* **116**, 172402 (2020). Copyright (2020) by Applied Physics Letters.

(b) "*The impact of metallic contacts on spin-polarized photocurrents in topological insulator Bi_2Se_3 nanowires*"
N. Meyer, K. Geishendorf, J. Walowski, A. Thomas and M. Münzenberg, *Appl. Phys. Lett.* **117**, 262401 (2020). Copyright (2020) by Applied Physics Letters.

(c) "*Observation of spin Nernst photocurrents in topological insulators*"
T. Schumann, N. Meyer, G. Mussler, J. Kampmeier, D. Grützmacher, E. Schmoranzerová, L. Braun, T. Kampfrath, J. Walowski, M. Münzenberg, submitted

(d) "*Circular photogalvanic effects in topological insulator/ferromagnet hybrid structures* "
T. Schumann, T. Kleinke, L. Braun, N. Meyer, G. Mussler, J. Kampmeier, D. Grützmacher, E. Schmoranzerová, K. Olejník, H. Reichlová, C. Heiliger, C. Denker, J. Walowski, T. Kampfrath, , M. Münzenberg, submitted

7 Acknowledgments

I wish to show my gratitude to everyone who encouraged and supported me during the last years and made this work possible. First and foremost, this is directed to Prof. Dr. Markus Münzenberg, who has been guiding me since I started working on my Master thesis. His helpful comments and suggestions allowed me to grow.

I would also like to acknowledge PD Dr. Andy Thomas and Dr. Kevin Geishendorf for the honest and forthright discussions and the successful collaboration regarding the topological nanowires.

Furthermore, I would like to thank my former and current colleagues of the AG Münzenberg, for their help and company in and out of the labs. Especially Dr. Jakob Walowski, who always has the time to discuss important and less important matters, shares his experimental knowledge open-handed and is quickly at hand with helpful comments and suggestions. This also applies to the technicians - Heidelore Bolt, Axel Knuth, and Jana Kredl - for their expertise and support in the lab and every shared laughter.

A special thanks is directed at Iris-Diana Passow for taking care of the administrative work.

In addition, I would like to thank my family and friends for their love and affection as well as happy distractions to rest my mind outside of my research.